Charles University in Prague
Faculty of Mathematics and Physics

DIPLOMA THESIS

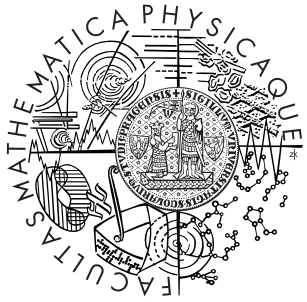

Pavla Doškářová

Determination of admixture of proton-antiproton pairs in DIRAC experimental data

Institute of Particle and Nuclear Physics

Supervisor: RNDr. Jan Smolík, Ph.D.

Study program: Nuclear and Subnuclear Physics

2009

Ráda bych poděkovala vedoucímu mé diplomové práce RNDr. Janu Smolíkovi, Ph.D. za vypsání tématu této práce, za inspirující a přínosné konzultace a za uvedení do problematiky exprimantu DIRAC a zpracování dat.

Dále moje díky patří panu Valeri Yaz'kovovi z Lomonosovovy Moskevské státní univerzity, který mi poskytl zpracovávaná data a který se mnou trpělivě konzultoval analýzu při mém pobytu v CERNu a tím ji pomohl udělat důkladnější a přesnější.

Prohlašuji, že jsem svou diplomovou práci napsala samostatně a výhradně s použitím citovaných pramenů. Souhlasím se zapůjčováním práce a jejím zveřejňováním.
Praha, 14.4. 2009 Pavla Doškářová

Název práce: Stanovení příměsi proton-antiprotonových párů v datech měřených experimentem DIRAC
Autor: Pavla Doškářová
Katedra (ústav): Ústav částicové a jaderné fyziky
Vedoucí diplomové práce: RNDr. Jan Smolík, Ph.D.
e-mail vedoucího: smolik@fzu.cz

Abstrakt: Hlavní cíl experimentu DIRAC je přesné měření párů $\pi^+\pi^-$, výběr "atomových" párů s malou relativní hybností ($Q < 3\mathrm{MeV/c}$) a určení pravděpodobnosti rozpadu, jak je popsáno v druhé kapitole této práce.

Experiment DIRAC se skládá z mnoha částí - terče, vakuové trubice, spektroskopického magnetu a různých detektorů. Více informací k jednotlivým částím nebo triggeru je uvedeno ve třetí a čtvrté kapitole.

Hlavní téma, kterým se v diplomové práci zabýváme, je určení příměsi $p\bar{p}$ párů v $\pi^+\pi^-$ párech a v celých experimentálních datech. Data, která byla použita, byla naměřena během roku 2001 na niklových terčích. Samotná analýza se nejprve zabývá zjištěním počtu protonů a antiprotonů v jednotlivých ramenech detektoru. Dalším krokem je určení hledaných $p\bar{p}$ párů v obou výše zmíněných případech a odpovídajících chyb.

Klíčová slova: experiment DIRAC, $A_{2\pi}$ atomy, pravděpodobnost rozpadu, $p\bar{p}$ páry

Title: Determination of admixture of proton-antiproton pairs in DIRAC experimental data

Author: Pavla Doškářová
Department: Institute of Particle and Nuclear Physics
Supervisor: RNDr. Jan Smolík, Ph.D.
Supervisor's e-mail address: smolik@fzu.cz

Abstract: The goal of the DIRAC experiment is precise measurement of the $\pi^+\pi^-$ pairs, the selection of "atomic" pairs with low relative momenta ($Q < 3\mathrm{MeV/c}$) and the determination of the breakup probability. These problems are described in the second chapter of this thesis.

Experiment DIRAC consists of many parts - the target, the vacuum channel, the spectrometer magnet and different detectors. More information about individual parts or the DIRAC trigger is mentioned in the third and the fourth chapter.

The main theme, which we engage in this diploma thesis, is to determine the admixture of $p\bar{p}$ pairs in $\pi^+\pi^-$ pairs and in whole experimental data. These data, which were analysed, were taken during 2001 on the nickel targets. The analysis deals at first with the determination of number of protons and antiprotons in individual arms of detector. The next step is the determination of $p\bar{p}$ pairs in both aforementioned cases with correspondig errors.

Keywords: the DIRAC experiment, $A_{2\pi}$ atoms, breakup probability, $p\bar{p}$ pairs

Contents

Chapter 1

Introduction

The experiment DIRAC (DImeson RElativistic Atomic Complexes) at CERN[1] uses the high intensity 24 GeV/c proton beam of the CERN Proton Synchrotron and its detector is magnetic double arm spectrometer.

DIRAC measures the lifetime τ of the $\pi^+\pi^-$ atom $A_{2\pi}$ to test low energy QCD prediction. As the lifetime is of order 10^{-15}s, it is determinated by probability annihilation $\pi^+\pi^- \to \pi^0\pi^0$ (more than 99%). The lifetime is related to relevant scattering length $1/\tau \sim |a_0 - a_2|^2$, where $|a_0 - a_2|$ is the combination of the s-wave $\pi\pi$-scattering lengths for isospin $I = 0$ and 2. The $\pi\pi$-scattering lengths a_0 and a_2 have been calculated within the framework of Chiral Perturbation Theory by means of an effective Lagrangian. The lifetime of the ground state is predicted to be $\tau = (2.9 \pm 0.1) \cdot 10^{-15}$s[2].

The method of the lifetime measurement is based on the production of the $A_{2\pi}$ atoms in a thin target and a subsequent detection of highly correlated $\pi^+\pi^-$ pairs leaving the target[3].

Pairs of $\pi^+\pi^-$ are produced as unbound ("free") pairs or with small probability as $A_{2\pi}$ atoms. The $A_{2\pi}$ atoms may latter either annihilate into $\pi^0\pi^0$ or break up into $\pi^+\pi^-$ pairs ("atomic" pairs) after interaction with target atoms. The observable relative momentum Q in these pairs c.m. system is $Q < 3$MeV/c for thin target ($\sim 10^{-3} X_0$).

The breakup probability of $A_{2\pi}$ atoms is an unique function of the atom momentum and depends on the dynamics of the $A_{2\pi}$ interaction with the target atoms and the $A_{2\pi}$ lifetime. The theoretical ionization probability for $A_{2\pi}$ atoms is obtained with a precision of 1% for a given target material, target thickness and momentum.

The value of brake-up probability established from DIRAC experiment includes statistic and systematic error. One of sources of systematic error is presence of unrecognized $p\bar{p}$ pairs which fulfilled all selection criteria. These $p\bar{p}$ pairs evocate decreasing of brake-up probability. The abundance of $p\bar{p}$ pairs is estimated to be around 0.15%. In this work we analyse data from year 2001 to find out real abundance of these pairs which is important for knowing the right affecting of brake-up probability by $p\bar{p}$ pairs. At first we deal with the analysis of proton, antiprotons and in the end with $p\bar{p}$ pairs.

Chapter 2

Theoretical background of DIRAC experiment

2.1 Motivation

Quantum Chromodynamics (QCD) is considered as the elementary theory of strong interaction. It is a perturbation theory with a running coupling constant. Due to an increasing value of the coupling constant with decreasing energy the theory can not be used at low energies. But we can use at low energies the Chiral Perturbation theory (ChPT).

ChPT describes the problem of pion scattering with high precision. We can calculate the theoretical value of the two $\pi\pi$-scattering lengths a_0, a_2 and their difference $\Delta = |a_0 - a_2|$ in the framework of ChPT[4].

$$a_0 = 0.220 \pm 0.005[m_\pi^{-1}] \tag{2.1}$$

$$a_2 = -0.0444 \pm 0.001[m_\pi^{-1}] \tag{2.2}$$

$$\Delta = |a_0 - a_2| = 0.265 \pm 0.004[m_\pi^{-1}] \tag{2.3}$$

As this theoretical prediction was done with a very high precision, there was a lack of experimental data for a long time.

At the time of preparation of DIRAC experiment the main thing was to measure the difference $|a_0 - a_2|$ with a 5% accurancy.

The value of a_0 was obtained from the detailed measurement of the decay $K \rightarrow \pi^+\pi^-e^+\nu_e$ by the E867 experiment at Brookhaven Alternating Gradient Synchrotron[5].

$$a_0 = 0.216 \pm 0.013(stat) \pm 0.004(syst) \pm 0.002(theor) \tag{2.4}$$

In this case a_0 was determinated with 6% precision.

Using a relation between a_0 and a_2 from the Chiral Perturbation Theory we can calculate a_2

$$a_2 = 0.0454 \pm 0.031(stat) \pm 0.001(syst) \pm 0.0008(theor) \tag{2.5}$$

2.2 Production of pion pairs at high energies

An inelastic collision of the protons from the 24GeV/c PS beam and the target atoms lead to $\pi^+\pi^-$ pairs production[6]. These $\pi^+\pi^-$ pairs can be of various origin. They can come from two different proton nucleus collisions or they can come from the same one with or without Coulomb final state interaction (FSI). These pairs can be uncorrelated (accidentals), time correlated without Coulomb FSI (non-Coulomb) and time correlated with Coulomb FSI in dependence on their origin. Atomic pairs are $\pi^+\pi^-$ pairs which origin from the breakup of $A_{2\pi}$ due to interaction with target atoms.

Pions that are produced close to each other, compared with the pionium Bohr radius ($a_\pi = 387 \cdot 10^{-15}$m), underlie Coulomb final state interaction. We label such pion pairs **Coulomb pairs**. These pairs are the dominant part of the background events. Their high production rate is confirmed experimentally by fitting the background events. Some of these pions will bind to each other with a certain probability by means of the Coulomb final state interaction leading to pionium, the $\pi^+\pi^-$ bound system (*Figure*2.1)).

While traveling through the target, the $A_{2\pi}$ atoms interact with the target nuclei and sometimes break up into atomic pairs, $\pi^+\pi^-$ pairs with Coulomb FSI. Their extraction is the goal of the DIRAC experiment.

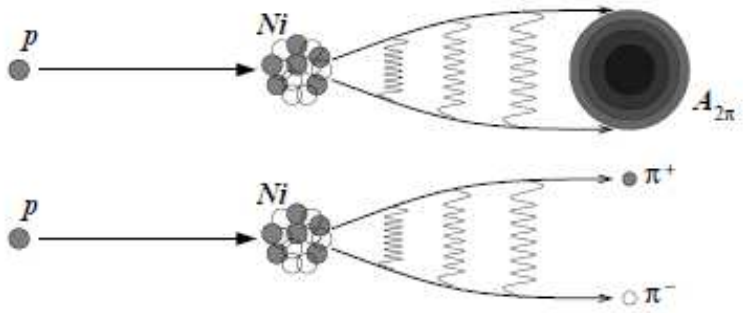

Figure 2.1: This figure shows the parallel production mechanism of atomic bound states (top) and free $\pi^+\pi^-$ Coulomb pairs (bottom).

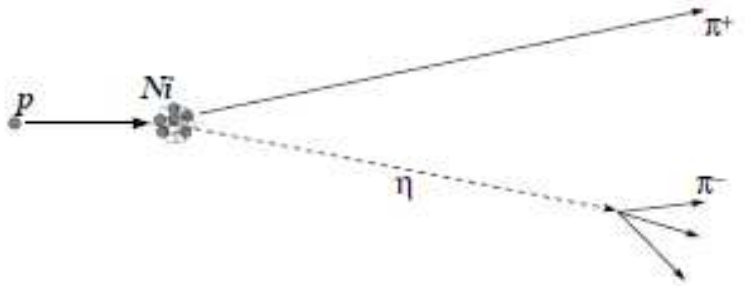

Figure 2.2: Production mechanism of non-Coulomb pairs.

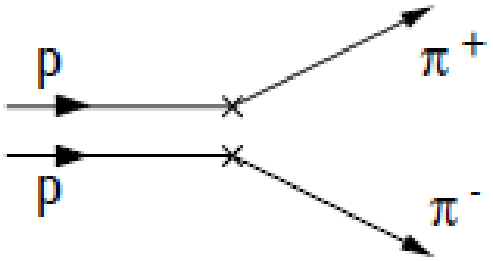

Figure 2.3: The production $\pi^+\pi^-$pairs in two proton nucleon interactions.

In addition to atomic and Coulomb correlated pairs non-Coulomb $\pi^+\pi^-$ pairs are also produced (Figure (2.2)). These are time correlated pairs, both pions come from the same proton-target interaction, where at least one of the pion is produced in the decay of long lived particles (e.g. η, K_S^0 or Λ)

Most of pions that are produced in the target are uncorrelated to each other. They origin from different proton nuclei interactions as shows Figure(2.3).

2.3 Breakup probability

The direct measurement of $A_{2\pi}$ lifetime is due to its very small value practically impossible. Therefore an indirect method based on the determination of $A_{2\pi}$ breakup probability P_{br} is used.

There is a small but finite probability that two opposite charged pions produced in a primary interaction will create the bound state - $A_{2\pi}$ atom. After its creation pionium is moving inside the target and can either decay into $\pi^0\pi^0$ or interact mostly with the electromagnetic field with the target atoms (The Coulomb interaction with the target atoms can be described in first approximation using the Born approximation, which considers only one photon exchange) and thus be excited , de-excited or broken-up.

The breakup probability P_{br} for $A_{2\pi}$ atoms is defined as a ratio of number of broken up atoms n_A and number of produced atoms N_A.

$$P_{br} = \frac{n_A}{N_A} \tag{2.6}$$

Due to very distinct features of $\pi^+\pi^-$pairs from broken-up $A_{2\pi}$ ($Q < 3$MeV/c and small opening angle), the n_A can be measured from the excess of $\pi^+\pi^-$pairs at very small relative momentum. As for N_A, it can be calculated using the relation between the two-pions production in continuous (free pions) and discrete (bound pions) spectrum.

The breakup probability is a function of the target nuclei charge, the target thickness and the atom lifetime (Figure(2.4)). The measurement of P_{br} thus allows to determine the $A_{2\pi}$ lifetime.

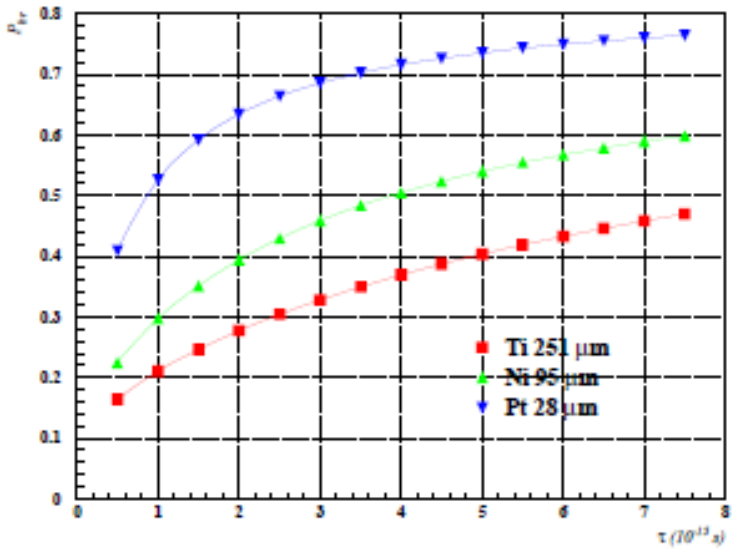

Figure 2.4: Breakup probability of $A_{2\pi}$ as a function of $A_{2\pi}$ lifetime for different target materials.

Chapter 3

DIRAC experimental setup

The DIRAC experiment is located at the T8 proton beam line 24GeV/c in East Hall of PS accelerator at CERN. It is designed for precise measurement of the $\pi^+\pi^-$ pairs and to select "atomic" pairs with low relative momenta. A calibration run was performed at the end of 1998. The DIRAC experiment has been collecting data since summer 1999. Its experimental setup was upgraded in 2006 and since than $K\pi$ atoms ($K^-\pi^+$ or $K^+\pi^-$) have also been measured. A detail description of DIRAC spectrometer is published in[7].

3.1 General layout description

The DIRAC detector is designed like double-arm spectrometer with main task to detect close $\pi^+\pi^-$ (or $K^-\pi^+$ or $K^+\pi^-$) pairs with high resolution. The DIRAC apparatus consists of a target station, the secondary vacuum channel, a spectrometer magnet and detectors which are placed upstream and downstream of the magnet.

The setup is very sensitive to backscattering particles. This is due to the fact that the target is very thin and the upstream detectors are placed closely to the target (around 20cm from the beam).

The secondary particle channel is positioned at an angle 5.7° upwards with respect to the primary beam (Figure (3.1)). The horizontal and vertical acceptance of the channel is ±1°. The upstream part consists of the following detectors : Microstrip gas chamber (MSGC), Scintillating fibre detector (SFD) and scintillation ionization hodoscopes (IH). The downstream part splits into two identical arms for the detection and identification of positive and negative secondary particles. The angle between the arms is $2 \times 19°$. There are Drift chambers (DC), Vertical and Horizontal hodoscopes (VH and HH), Cherenkov counters (CH), Preshower detector (PSH) and Muon counters (MU) (Figure (3.2)) along each arm.

3.2 Proton beam and target station

The protons are extracted from PS to T8 beam line in a slow extraction mode with the spill duration between 400 and 500ms. The intensity can be varied from 0.5×10^{11} to 3×10^{11} protons per spill. The Nickel target data were measured in 2001 and at the time

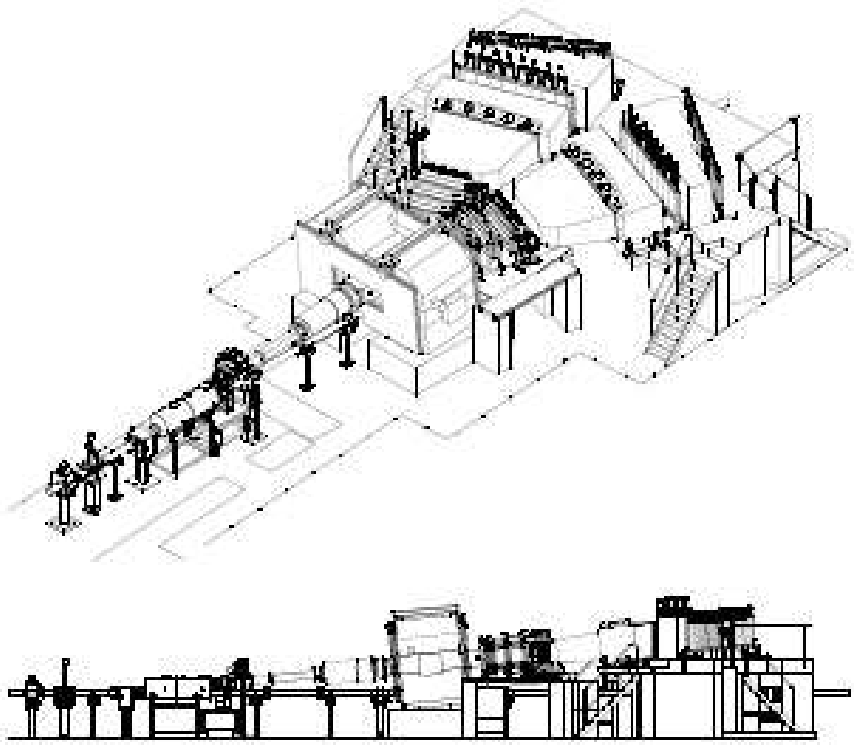

Figure 3.1: Isometric and side view of the DIRAC apparatus. The secondary particle channel is inclined by 5.7° with respect to the proton beam.

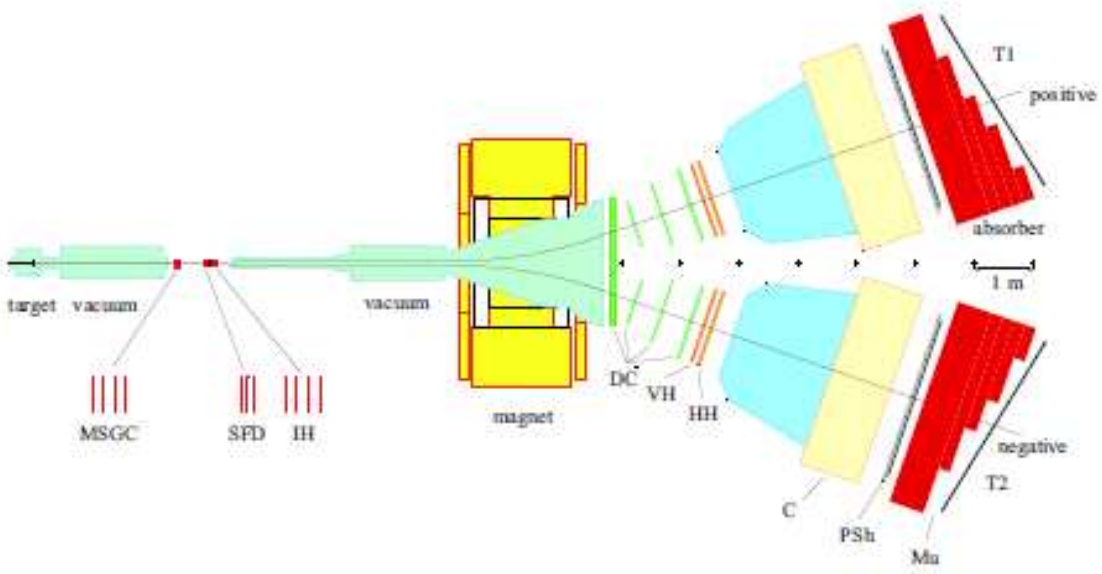

Figure 3.2: Top view of the setup. Detectors: Microstrip Gas Chambers (MSGC), scintillating fiber detector (SFD), ionization hodoscope (IH), magnet, drift chambers (DC), vertical hodoscopes (VH), horizontal hodoscopes (HH), Cherenkov detectors (C, or CH), preshower detectors (PSH) and muon counters (Mu).

the beam intensity was about 1×10^{11}. The beam dimensions at the target location are in vertical direction $x = 1.6$mm and horizontal direction $y = 3.2$mm at 2σ level.

The primary beam continues to flow after leaving the target station in a vacuum line below the spectrometer until a beam dump. The line and the beam dump are use to decrease background in detectors (The detector's counting rates are $\sim$ 25 times higher when a target is in palace than with the target out of place.).

The vacuum target station houses a device with 12 holders for targets which can be remotely change.

3.3 Upstream detectors

The upstream detectors are placed close to the target. Their main task is a precision measurement of close particle tracks with high detection rate and efficiency. The Microstrip gas chamber (MSGC), the scintillation fiber detector (SFD) and the ionization hodoscope (IH) are used to improve the precision of the relative pairs momenta. SFD and MSGC are essential to provide the coordinates of the effective beam position used in the momentum reconstruction. Both SFD and IH are also used in high levels of the trigger.

3.3.1 Microstrip gas chamber detector

The Microstrip gas chamber detector (Figure (3.3)) is placed at a distance of 2.4m from the interaction point. The detector consists of 4 planes. These 4 planes have an orientation of 0°, 90°, 5° and 85° with respect to the plane perpendicular to the secondary beam. The total number of channels is 2048. Each plane covers an active area of 10.24×10.24cm^2 and consists of a drift electrode, a GEM foil and a MSGC sensor.

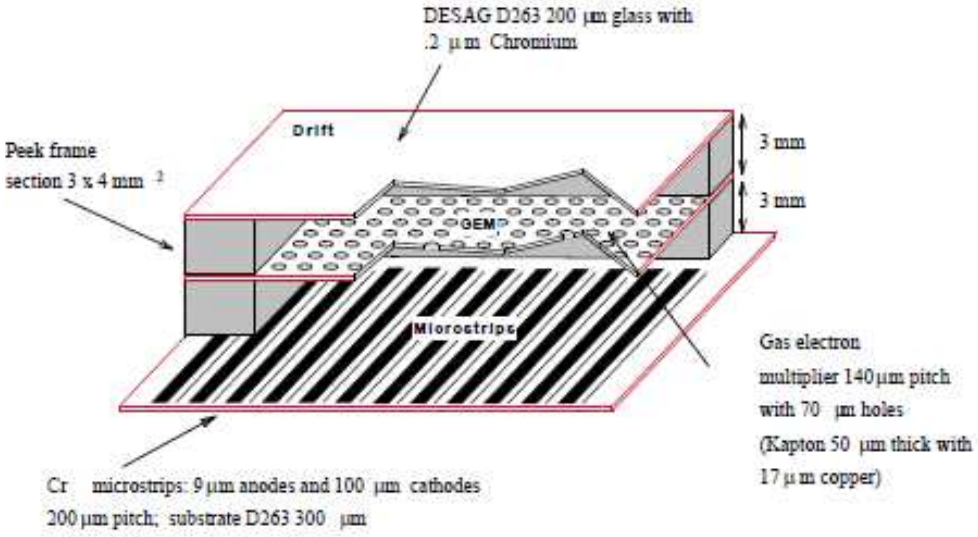

Figure 3.3: Layout of the MSGC detector.

The MSGC are operational since 2001 with an "off-time" of typically 40%. The efficiency per plane was measured to be around 93% which yields an efficinecy for all four planes of 75%. The single hit resolution is 54μm[7].

This detector is important to obtain a resolution in the transverse components of the pion pairs c.m.s. relative momentum below 1MeV/c.

3.3.2 Scintillation fibre detector

The scintillation fibre detector is used for tracking upstream of the magnet and triggering. The detector is placed at a distance of 2.95m from the target. It consists of 2 perpendicular planes (X and Y) separated by 2.5cm. Each plane has 240 channels. Since 2002 a third inclined U plane with 340 channels was added. The U plane is rotated with respect to the X axis by an angle of 45°. SFD covers an active area of $105 \times 105\text{mm}^2$.

Each column of X and Y planes consists from five scintillating fibres (with length of 130mm and diameter of 0.50mm) and each column creates one channel of a positive sensitive photomultiplier (PSPM). There are 16 channels per PSPM and 15 PSPM to yield all the 240 channel per one plane. The fiber column pitch is 440μm which defines the single track resolution (Figure (3.5)).

U plane consists, in contrast to X and Y plane, of just 3 layers of scintillating fibres with a higher diameter of 0.57mm. There are 320 active columns in 5 sections of different fibre lengths (150, 130 and 70mm).

SFD performance is influenced by the high flux of particles at the position of detector near the interaction point and by particles which are scattered toward the detector. The single track inefficiency is estimated to be 5%, for double ionization events with 2 tracks requirement the efficiency is about 91%. The time resolution is found to be around 0.8ns which translates into a relative time resolution between the two planes of about 1.2ns (Figure 3.4). The space resolution for single track events is given by the typical fiber pitch size that is 440μm. Double track resolution is distorted for close-lying tracks due to PSC (peak sensing circuit) behavior[7].

3.3.3 Ionisation hodoscope

The recognition of close tracks is crucial for the DIRAC experiment. The dedicated ionization hodoscope was built to separate single track hits from double close-lying tracks by take to account their ionization energy losses.

The described IH detector (Figure (3.6)) was installed in 2001 to replace old one. It is placed at a distance of 3.05m from the target. The detector consists of two X and Y planes with a sensitive area of $11 \times 11\text{cm}^2$. Each plane is covered by 16 plastic scintillator strips. One strip has a width of 7mm, a length of 11cm and a thickness of 1mm. They are connected to the PM (photomultiplier) photo cathodes with 2mm thin and 7mm wide lucite light guide. The nonsensitive gap between the strips is less than 70μm wide.

The ADC and TDC signal of IH are read out and are available during the off-line analysis. The ADC spetra for single and double ionization events are in Figure (3.7). If the threshold is set to retain 95% of double ionisation signal, the contamination of single

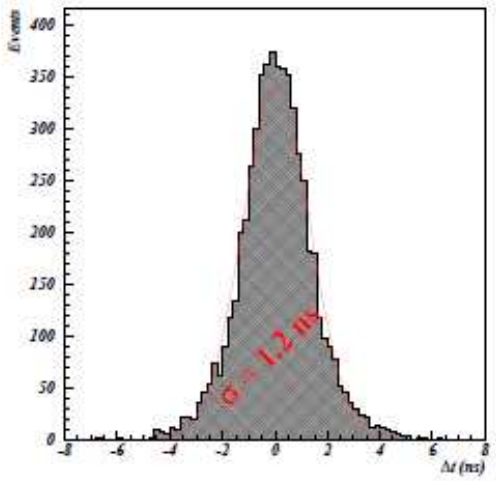

Figure 3.4: Time difference between the two SFD planes for reconstructed single track event.

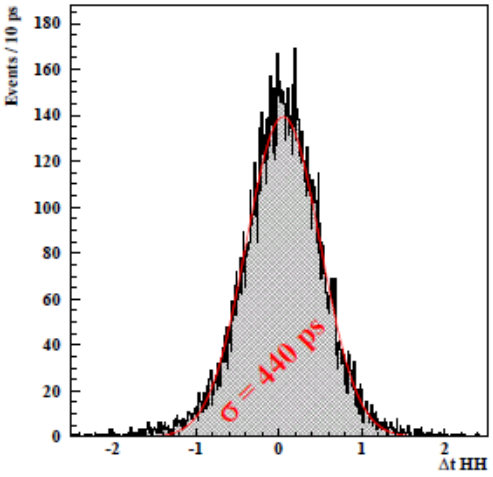

Figure 3.5: Time difference of the two arms for tagged pion pairs for 2001. The σ of the fitted Gauss function for the prompt signal is 440ps.

particle amplitudes is less than 15%. The time resolution between the VH and the first X plane of IH is better than 1ns (Figure (3.8)).

3.4 Magnet

The dipole spectrometer magnet is placed at a distance of 8.5m from the target. It separates positive and negative particles from the upstream area. Its magnetic field is 1.65T ($BL = 2.2$Tm). The magnet dimensions are $1.55 \times 0.50 \times 1.1\text{m}^2$ ($W \times H \times L$). The magnetic field was measured and parametrized to allow precise reconstruction of track of particles with different momenta[8].

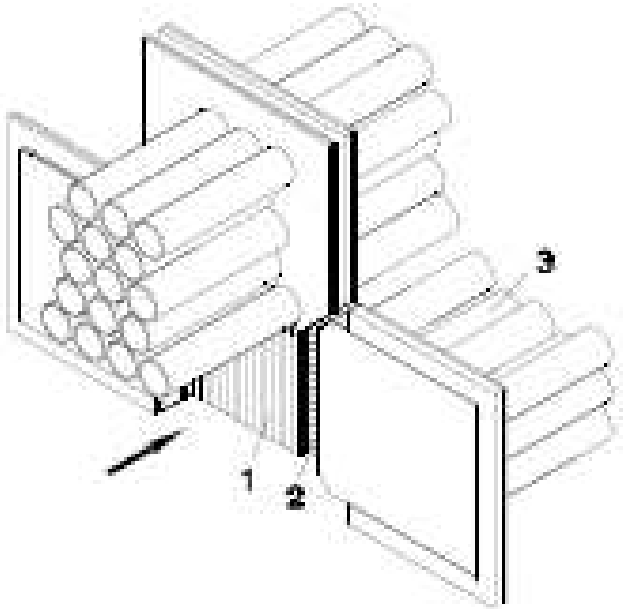

Figure 3.6: Isometric view of the Ionisation Hodoscopes. 1 scintillators, 2 light-guides, 3 photo multipliers with shielding.

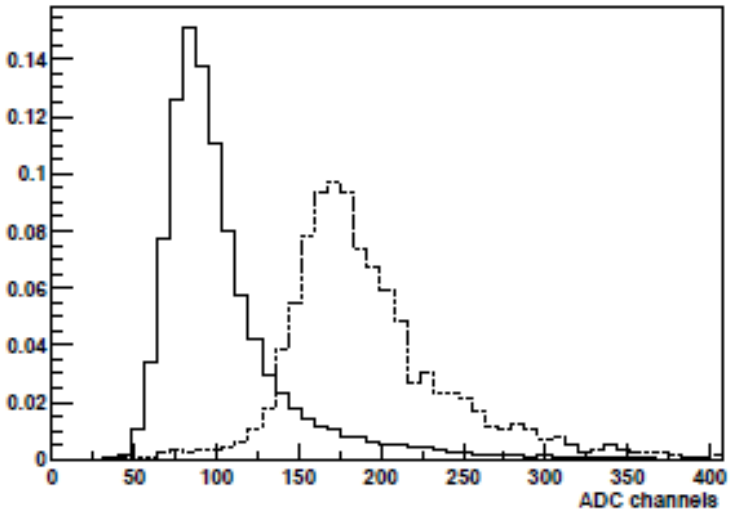

Figure 3.7: Typical ADC spectra for single (solid line) and double (dashed line) ionization loss from particles crossing one IH scintillating slab.

3.5 Downstream detectors

The downstream detectors form two arms of DIRAC experiment. The axes of symmetry of both arms are 19° to the left and to the right relative to the Z axis. The acceptance area covered by each arm is 11°. The detectors have several tasks: the measurement of space parameters of track behind magnet (Drift chambers - DC), identification of electrons and muons (Cherenkov counters - CH, Preshower detector - PS and Muon detector - MU) and

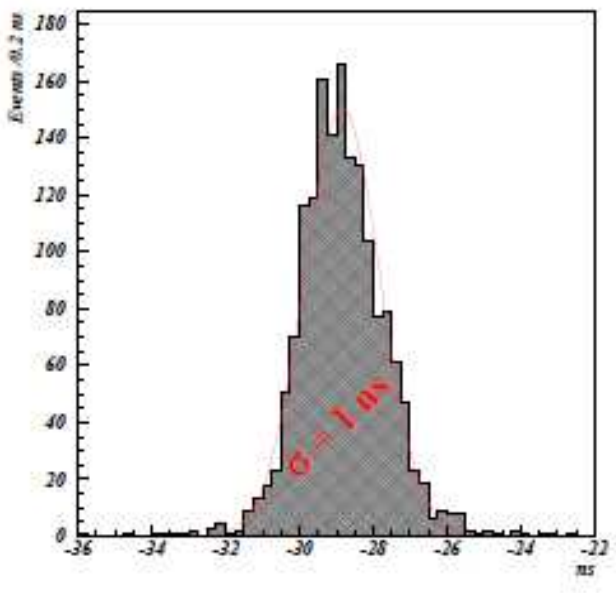

Figure 3.8: The time resolution between the VH and the first X plane of IH is about 1ns.

fast triggering and time measurement (vertical and horizontal hodoscope - VH and HH).

3.5.1 Drift chambers

The drift chambers system is used to perform particle tracking downstream the spectrometer magnet. It is designed to handle high particle flow up to 10kHz/cm^2. The drift chambers system is separated into seven independent modules. The first one (DC1), which is closest to the magnet, is common to positive and negative arms and consists of 6 chamber planes arranged in the X-Y-W-X-Y-W sequence. The W is rotated 11.3° with respect to the X axis. The DC1 has two separated sensitive area of 0.8×0.4m^2 each and is instrumented by 800 electronic channels.

Each arm is further equipped with three chambers, performing the measurement of X,Y (DC2), X,Y (DC3) and X,Y,X,Y (DC4). Their sensitive areas are 0.8×0.4m^2 (DC2 and DC4) and 1.12×0.4m^2 (DC3). Both arms contain together 1216 electronic channels.

A schematic drawing of the sensitive element is depicted in Figure (3.9). The anode wires pitch is 10mm, the distance between the anode and cathode planes is 5mm. The sensitive area has a square shaped area of 10×10mm^2. It is possible to achieve an almost linear behavior of the drift function with a suitable gas mixture except for a small region near the anode wire.

The chambers are operated in a high current avalanche mode (the chamber operation voltage is 3.85kV) which is characterized by high pulse amplitudes, small pulse and stable operation. The gas, that is used, consists of $Ar(\sim 50\%) + iC_4H_{10}(\sim 50\%) + H_2(0.5\%)$.

The resulting coordinate resolution of the DC system is measured to be around 100μm. The measured space resolution of 100μm also takes into account the uncertainty due to the track prediction so that the space resolution of the chamber alone is better than

90μm. The track efficiency of one chamber is about 99% and the track efficinecy of the DC system as a whole is about 99%.

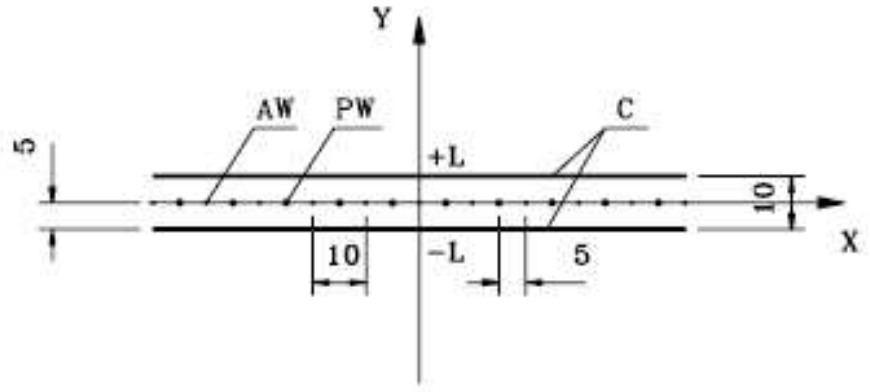

Figure 3.9: Schematic view of the wire chamber electrodes: AW anode wires, PW potential wires, C cathode foils. Dimensions are in mm.

3.5.2 Vertical hodoscope

The vertical hodoscope is designed to achieve a very high resolution to be able to distinguish between the particle pairs from one primary proton interaction and the particles produced at two different primary interactions. It is used in the first level trigger and in the DNA trigger to select good events.

Two VH (one per arm) are placed at a distance of 11.6m from the target and downstream the DC system. Their sensitive area is $0.4 \times 1.3\text{m}^2$. Each of hodoscopes consists of 18 vertical scintillation slabs with a length of 40cm, a width of 7cm and a thickness of 2.2cm. Scintillation light is collected at both ends of slab by two photomultiplier. The voltage dividers are designed to operate in a high particle rates up to 2MHz without any degradation of the time resolution.

The VH single-hit detection efficiency was estimated to be 99.5% for the positive arm and 98.8% for the negative one.

The time resolution can be estimated by electron pairs created in γ conversion or Dalitz diagram of π^0, which are almost synchronous at the time, because the time-of-flight of the electron is momentum independent in the available momenta acceptance. Figure (3.11) shows the time difference between the vertical hodoscopes for these time-correlated electron pairs. The fitted width of distribution is around 180ps. The intrinsic absolute time resolution per slab is therefore around of 120ps[9].

The time difference between events with pion flag is in Figure (3.10). The time-correlated prompt peak has the fitted width of approximately 193ps. The flat background is composed of time uncorrelated pairs, which do not originate from one primary beam interaction. On the right side of the peak is the effect of admixture of $\pi^- p$ pairs.

Figure (3.12) shows the time difference between the VH and the momentum of the positive particles. The vertical line results in time-correlated $\pi^+\pi^-$ pairs, while the curve

lines originate from $\pi^- p$ pairs in the momentum range from 1 to 5GeV/c and from $\pi^- K^+$ pairs in the range from 1 to 2.5GeV/c.

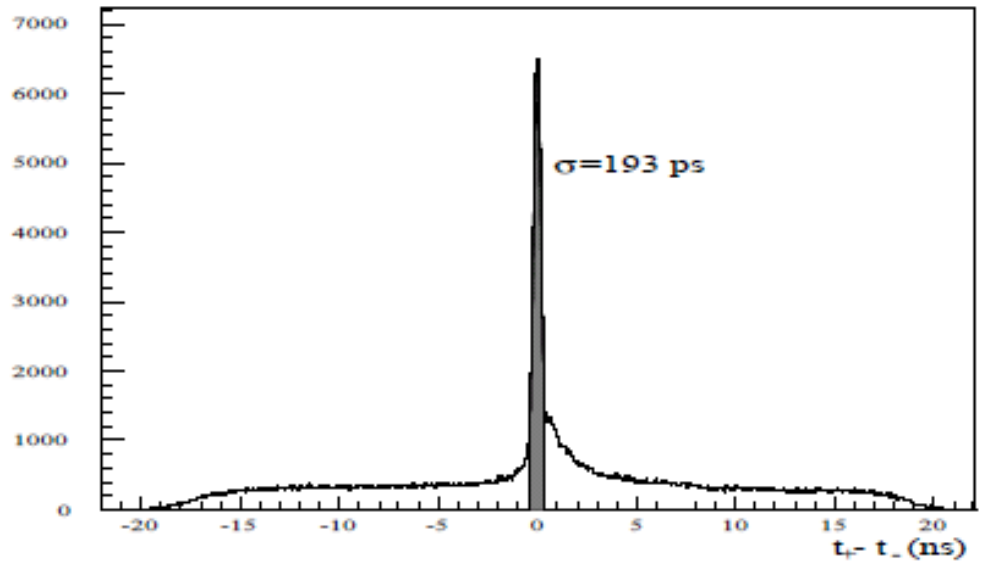

Figure 3.10: Time difference charged particles measured by the vertical hodoscope planes in the positive and negative arms of the spectrometer. The central peak has a Gaussian width of 193ps and the shaded area corresponds to 2σ where the signal and prompt background events are found. The shoulder on the right side of the peak is due to the $\pi^- p$ prompt pairs.

3.5.3 Horizontal hodoscopes

The Horizontal hodoscopes system (Figure (3.13)) is, just like the VH, separated into two arms. Each of them covers an active area of $130 \times 40\text{cm}^2$ and consists of 16 independent scintillating slabs in horizontal direction. Slabs dimensions are $130 \times 2.5 \times 2.5\text{cm}^2$ ($L \times W \times T$). Their ends are connected into photomultipliers which are equipped with voltage dividers to allow high counting rate capability.

A positive answer is required from HH for each arm for the first level trigger and its response is also used to select events with small relative opening angle in the y direction.

The single hit detection efficiency of HH is better than 96.6% for both arms and the absolute intrinsic time resolution per slab is around 320ps[9]. It is worse than for VH due to the greater length of slabs.

3.5.4 Cherenkov counters

The Cherenkov radiation occurs when the velocity of the charged particle exceeds the velocity of light in a dielectric medium. A charged particle polarize atoms which results

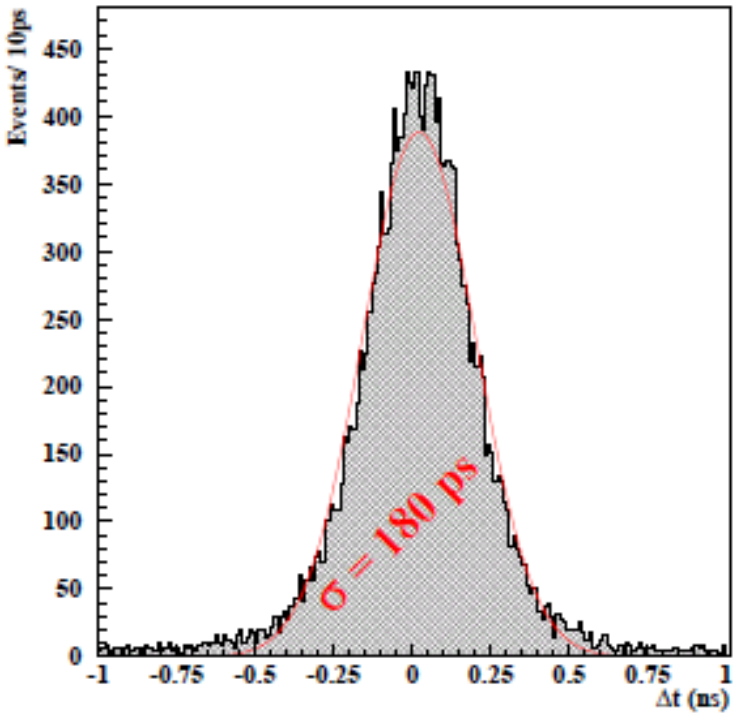

Figure 3.11: Time difference of the two arms for prompt electron pairs measured in 2001. The Gaussian width is 180ps.

characteristic emission of coherent radiation. The angle of direction of the emitted light is related to the particle's velocity β and the index of refraction n

$$cos\theta = \frac{1}{\beta n}. \tag{3.1}$$

The most charged particles detected by the Cherenkov counter in our experiment have a value of β close to 1. For this reason a material with a low index of refraction (as gas) is required. Nitrogen at normal temperature and pressure is used in our experiment as the gas radiator ($\theta = 1.4°$).

The Cherenkov counters play a crucial role in rejection of electron-positron pairs from photon conversion, Dalitz diagram of π^0 and are therefore essential to suppress a major source of background. The response from the Cherenkov counters is used in the first level $\pi^+\pi^-$ trigger and in the calibration e^+e^- trigger.

They consist of two identical threshold Cherenkov detectors located in distance of 11.8m from the target. Each detector covers one spectrometer arm. The counters are 285cm long and their dimensions are $0.56 \times 1.43\text{m}^2$ and $0.96 \times 3.36\text{m}^2$, respectively.

Each counter is equipped with 20 mirrors and 10 photomultipliers in two rows. Light from two adjacent mirrors is reflected in the same photomultiplier. The mirrors are spherically deformed rectangles with dimensions of $30 \times 35 \times 0.6\text{cm}^3$. The analog signals from individual photomultipliers are fed into two custom-made summing modules, one per arm. The output of the summing module is a linear sum of the input channels. The

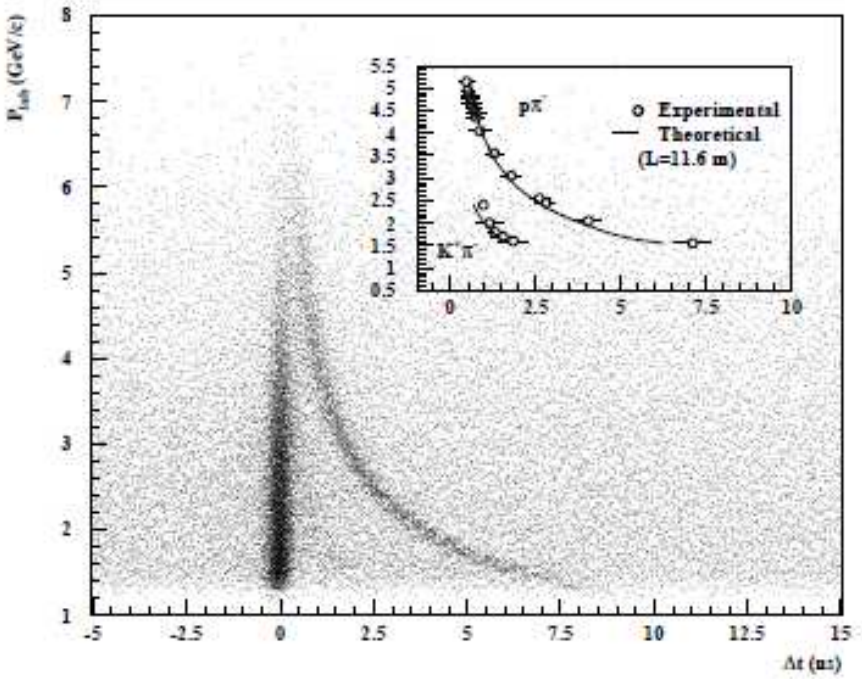

Figure 3.12: Correlation between the measured momentum of the positive particle and the VH time difference between the positive and negative spectrometer arm, taking into account the correction for the difference in path length. The accumulation bands correspond to $\pi^-\pi^+$ (vertical band) and $\pi^- p$ (curved band) pairs. A small cluster of $\pi^- K^+$ pairs is also visible in the intermediate region.

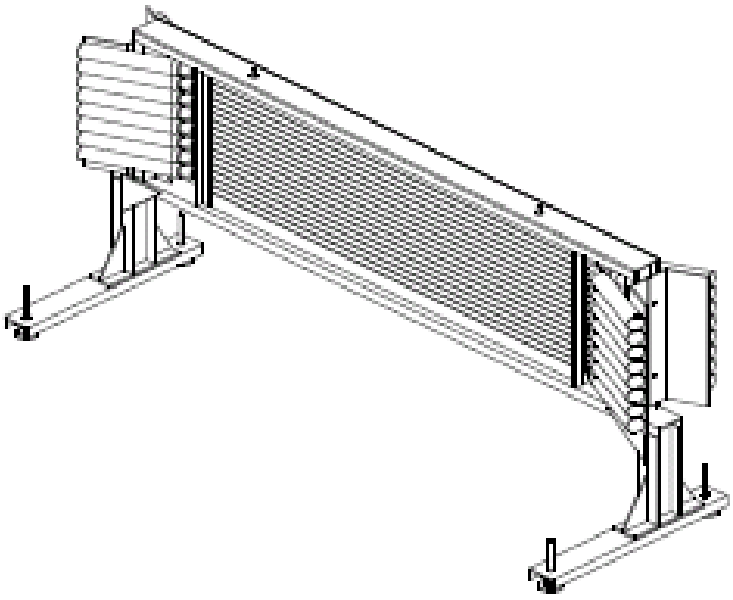

Figure 3.13: Picture of the Horizontal hodoscope.

sum and signals of individual photomultipliers are fed into ADC units and are available for off-line analysis and the detector tunning.

Both counters have an efficiency greater than 99.8% and the pion contamination above the detection threshold is less than 1.5%[7].

3.5.5 Preshower detector

The Preshower detector is used in the low level trigger and during off-line analysis allows additional elimination of electron background that are not recognized by the Cherenkov detector.

It is placed at a distance of 15.4m from the target and in each arm covers a sensitive area of $0.75 \times 2.8\text{m}^2$.

The PSH (Figure (3.14)) is built as an array of 8 elements per arm. Each element has a lead converter and scintillation counter placed behind it. The converters of the two furthermost elements are 10mm thick while the others are 25mm thick. It corresponds to 2 and 5 unit of radiation length. The scintillation counters are $0.75 \times 0.35\text{m}^2$ large and 1cm thick. Each of counter is connected through a light guide to photomultiplier.

The detector concept is based on a different behaviour of electrons and pions in matter. Electrons which pass through the lead converter shower electromagnetically while pions behave mainly as minimum ionization particles. The resulting energy losses are measured by scintillators and depend on a species of a particle.

The single arm detector efficiency is 99.5% for pions. The off-line analysis shows that rejection of electrons reaches 85% with less than 5% losses of pions. The combined information from CH and PSH provides almost 100% rejection of electrons.

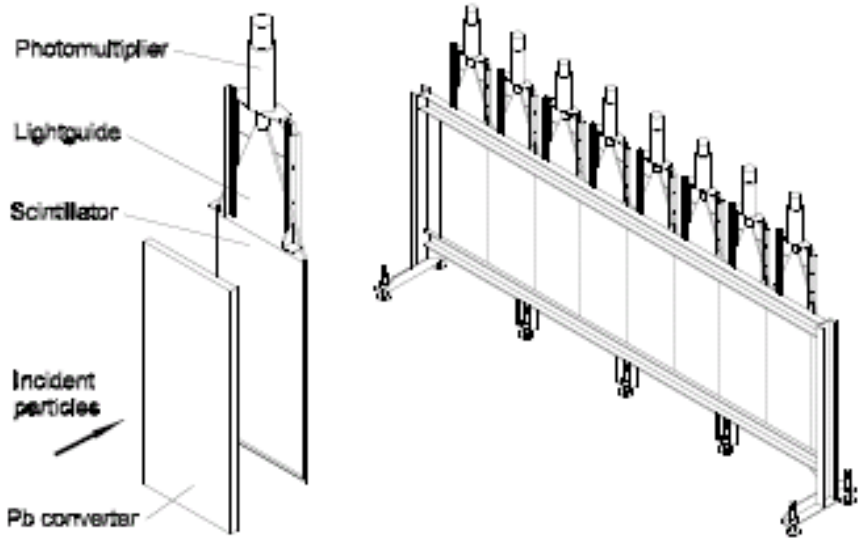

Figure 3.14: Preshower detector concept for one element and one spectrometer arm.

3.5.6 Muon detector

The muon counters are designed to suppress background from muons. Most of the muons originate from pion decays and with only a small fraction from other decays and direct $\mu^+\mu^-$ production.

The detector is placed at 16.5m distance from the target. It is built from scintillation counters which are placed behind a thick iron absorber. This absorber almost entirely absorbs hadrons and related hadron showers and allows only muons to fly through. The iron absorber thickness ranges from 60 to 140cm. The thickness is larger in the region close to the spectrometer axis in order to compensate for the higher particle momenta.

The muon counters (Figure (3.15)) are installed symmetrically and are built as a double layer structure. Each layer consists of 28 counters with equal scintillating slabs of $75 \times 12\text{cm}^2$ in size and 0.5cm thick. The registered data are read out only if there are responses from both layers. This condition significantly decreases the number of dummy signals.

The scintillation light is guided to photomultiplier at one end of the counter. Signals from both layers are fed into a constant fraction discriminator followed by a meantimer.

The time resolution of the muon counter is around 1.3ns. The fraction of events which contain at least one muon was estimated to be around 10%. Such muons events originate mostly ($\sim 80\%$) from $\pi^{\pm}$ decays between DC and Muon counters[10].

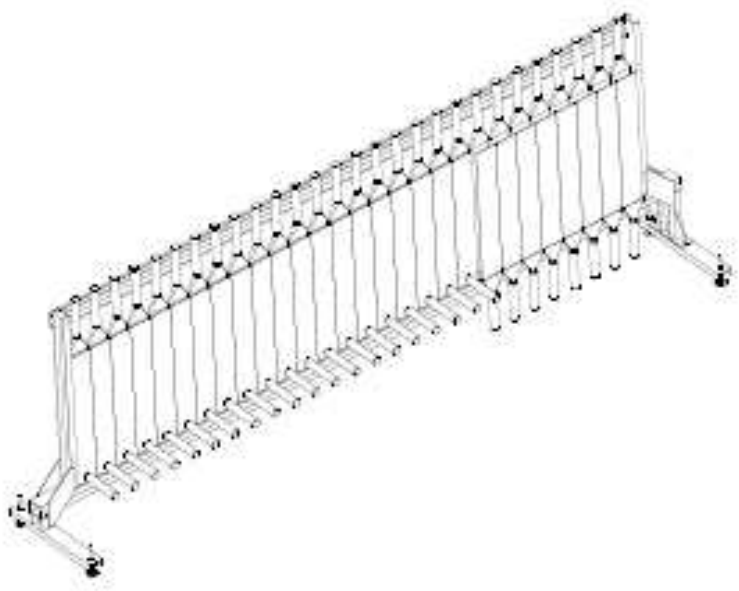

Figure 3.15: Schematic layout of muon counters on their support structure, indicating light guides and photo multipliers.

Chapter 4

DIRAC Trigger

The secondary particles resulting from PS proton beam-target atoms collisions results in single count rates a few times 10^5 counts/sec in the downstream detectors to a few times 10^6 counts/sec in the upstream detectors. The processing capability of the data acquisition system is around 2000 event/spill. It is essential for the trigger system capability of rate reduction of around 1000 to have. The DIRAC experiment has a very sophisticated multilevel trigger. In addition to a very fast level trigger, there are two higher level triggers. Due to the very specific data analysis procedure, the DIRAC trigger has to select not only time correlated events - such as pions originating from $A_{2\pi}$ - as well uncorrelated $\pi^+\pi^-$ pairs. The optimal ratio of time-correlated to time-uncorrelated events is achieved by using a time window of coincidence of $\pm$20ns between tracks in the positive and the negative arm. Specifically the time coincidence is obtained by the vertical hodoscopes.

The trigger system has been upgraded since the start of operation in 1999 several times. The detailed description of DIRAC trigger is in [7][11] and the trigger performance was studied in detail in [12].

4.1 Trigger scheme

The general trigger scheme is shown in Figure (4.1). The zero level trigger (T0) actives neural network level of trigger (DNA). The first level trigger (T1) starts digitisation of the detector signal in the data acquisition modules (ADC, TDC). The drift chamber trigger processor (T4) starts with a positive decision from T1. The positive decision of DNA in coincidence of T1 is used again in coincidence with the decision of T4. If the result is positive, the readout of all detectors starts. If not, the buffers are cleaned. These two stage processes are chosen to minimize the trigger decision time and dead-time due to long readout time of MSGC. The readout of MSGC starts immediately after DNA decision.

In addition to the main trigger task to detect atomic pairs, there are several additional calibration triggers which can run simultaneously or separately. When the specialized calibration triggers are running simultaneously with the main trigger, the appropriate prescalling factors are used.

The whole trigger system is fully computer controlled and no hardware intervention is needed to change the trigger configuration. The average number of accepted events per spill under typical experiment condition is 700.

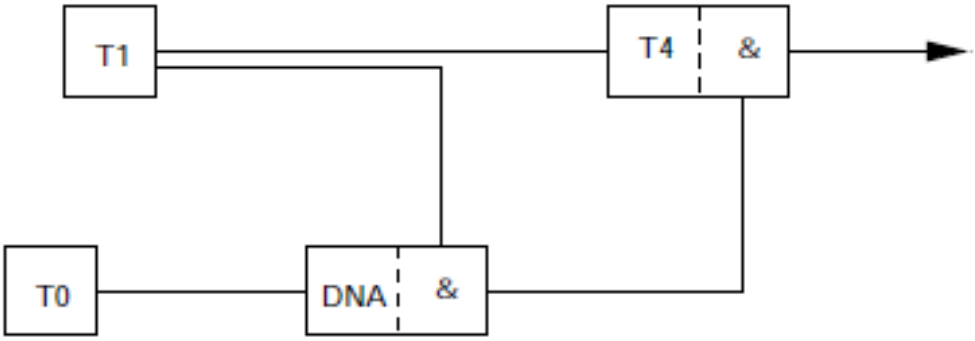

Figure 4.1: General block diagram of the DIRAC multilevel trigger.

4.2 Zero level trigger T0

The T0 trigger is introduced to obtain very early initial signal for DNA trigger. It is defined as a coincidence between Vertical hodoscope and Preshower detector for the left and right arm.

$$VH_1 \cdot PSH_1 \& VH_2 \cdot PSH_2 \tag{4.1}$$

where 1,2 denotes the positive and negative arm. The coincidence window defined as the time difference between a pair of hit slabs in the negative arm and the trigger hit in the positive arm of each detector is set at ±20ns.

4.3 First level trigger T1

The T1 trigger allows to make a fast coincidence among downstream detectors and it as well ensures the timing is precise. Specifically it performs the following tasks:

- Selects events with signals in both detector arms downstream the magnet in the time window of ±20ns. The signal from Vertical hodoscope is used for timing.
- Classify the particles in electrons and pions. Kaons, protons and muons are also flagged as pions, but their identification is performed in the off-line analysis using the time of flight information and a dedicated muon counter detector.
- Applies a cut on vertical opening angle (Complanarity cut) for pion pairs. The cut requires that the difference between hit slabs in the horizontal hodoscope in the two arms is less than three.
- Selects additional calibration events : $e^+e^-, \Lambda \to p + \pi^-$ decays and K decays into three charged pions ($K^+ \to \pi^+\pi^+\pi^-, K^- \to \pi^-\pi^-\pi^+$)

Pion signature - To mark registered pion track in one arm the signal from the downstream detectors must agree with following mask:

$$VH_i \cdot HH_i \cdot \overline{CH_i} \cdot PSH_i (i = 1 \text{ or } 2) \tag{4.2}$$

which means that hits must be registered in the vertical and horizontal hodoscopes and the preshower detector but not in Cherenkov detector.

Electron signature - The mask for electrons is:

$$VH_i \cdot HH_i \cdot CH_i \cdot PSH_i (i = 1 \text{ or } 2) \tag{4.3}$$

The signature is a coincidence of a hit in vertical, horizontal hodoscopes, Cherekov detector and Preshower detector.

The decision from both arms are combined to produce the final T1 decision for pion pairs ($\pi^+\pi^-$) and for electron pairs (e^+e^-). The electronic of the T1 trigger gives a result within 120ns. The vertical hodoscope is used to define the timing of tracks and to establish time coincidence window.

Λ **signature** - In addition to pion and electron pairs signatures, T1 trigger accepts events which are likely to come from a Λ decay $\Lambda \rightarrow p + \pi^-$. Due to asymmetric kinematic of Λ decay the mask is following:

$$(VH_1(17) \cdot HH_1 \cdot \overline{CH_1} \cdot PSH_1) \& (VH_2(1-16) \cdot HH_2 \cdot \overline{CH_2} \cdot PSH_2) \tag{4.4}$$

For vertical hodoscope only the slab 17 is used in the positive arm while for the negative arm the slabs from 1 to 16 are looked at. The coincidence window is reduced to $\pm$2.5ns.

K **signature** - Label three hits in vertical and horizontal hodoscope are demanded for kaon. At least one hit must be registered in each arm. The coincidence window is wider than for Λ mark and is $\pm$5ns.

4.4 Neural network trigger DNA

The DIRAC neural network trigger[13] is a processing system which uses a neural network algorithm. DNA receives as input the hit patterns from VH1, VH2 and X-planes of the upstream detectors IH and SFD. DNA is able to cope with up to two hits in each VH1 and VH2 and up to five hits per X-plane of IH. Events with more hits are accepted for off-line evaluation. Each X-plane in conjunction with the input signal from the two VH are evaluated independently and simultaneously. An event is accepted if the trigger decision is true at least for one X-plane. This scheme eliminates influences of dead spaces between slabs of IH X-planes.

DNA was trained to select pairs with low relative momenta: $Q_x < 3$MeV/c and $Q_L < 30$MeV/c. The training was performed on Monte Carlo simulated data and then rechecked with real experimental data. The DNA starts with a T0 signal and processes an event in about 210ns. In a second step its decision is put in coincidence with that one from T1 so that only events that have a positive decision from T1 and DNA are further processed. The DNA rejection rate is about 2.3 with respect to T1 and the efficiency for the low Q region is of the order of 94% .

4.5 Fourth level trigger T4

The T4 is the final stage of the trigger. It uses the drift chamber information to reconstruct straight tracks in X-direction which allows to estimate the Q_x projection of pair relative momentum.

T4 processor includes two stages: the track finder and the track analyser. The T4 track finder evaluates hits from all X-planes of the drift chambers to find straight tracks. Each track is assigned a unique number "track identifier". If at least one track is found in each arm, the track analyser continues to evaluate the event. If T4 receives the track identifiers from both arms and compares them with the content of the look-up memory table and issues the a positive or negative decision. The look-up table is constructed from measured data and includes all possible patterns coming from tracks with relative momenta of $Q_x < 3$MeV/c and $Q_L < 30$MeV/c. This table was obtained from the dedicated simulation using the precise geometry of setup.

The T4 decision time varies depending on the complexity of the event. The decision time is from 1.5μs for simple events to more than 20μs for the more complicated ones. The average is around 3.5μs. The T4 rejection factor is about 5 with respect to T1 and around 2.5 with respect to DNA.

The T4 efficiency for $Q < 30$MeV/c exceeds 99%.

Chapter 5

The first data

5.1 Identification of data

The analysed data was processed from raw data taken in 2001 with aim to study admixture of K mesons. It was done by Valeri Yaz'Kov, the physicist who deals with data analysis in DIRAC experiment. The selected data have standard T4 trigger mark. To avoid muons the events with one or more corresponding hits in muon detectors were rejected. To have cleanly reconstructed events the additional cuts were applied on the information from upstream detectors. At least hits in two planes of IH for each track and two separated hits in fibre detector are demanded. The last criterion suppress pairs with Qx and Qy less then 4 MeV/c effectively (Q - relative momenta of particles). The information from MSGC detector is not used.

For each event the following information is available:

- $\mathrm{T}_{\pi/K,-/+}$, *time difference between expected and measured time of flight in case that particle is π - pion or K - kaon between Vertical hodoscope and upstream detectors (Scintilation fibre detector and Ionization hodoscope) for $-$ negative or $+$ positive arm,*
$$T_{\pi/K,+/-} = T_{teor\,\pi/K,+/-} - T_{measured,+/-} \tag{5.1}$$
- $\mathrm{P}_{-/+}$, *a momentum of $-$ negative or $+$ positive particle,*

from these variables is calculated

- $\mathrm{T}_{P,-/+}$, *time difference between expected and measured time of flight in case that particle is p - proton between Vertical hodoscope and upstream detectors (Scintilation fibre detector and Ionization hodoscope) for $-$ negative or $+$ positive arm.*

$$T_{P,+/-} = T_{teor P,+/-} - T_{measured,+/-} \tag{5.2}$$

$$T_{measured,+/-} = T_{teor\,\pi,+/-} - T_{\pi,+/-} \tag{5.3}$$

$$T_{teor\,\pi/K/P,+/-} = \frac{L_{+/-}}{\beta_{\pi/K/P,+/-} * c} \tag{5.4}$$

$$\beta_{\pi/K/P,+/-} = \frac{P_{+/-}}{\sqrt{m^2_{\pi/K/P} + P^2_{+/-}}} \tag{5.5}$$

$$L_{+/-} = \beta_{\pi,+/-} * \beta_{K,+/-} * c * \frac{T_{teorK,+/-} - T_{teor\,\pi,+/-}}{\beta_{\pi,+/-} - \beta_{K,+/-}} \tag{5.6}$$

From figures (5.1) and (5.2) one can see the momentum distributions of particles for individual arms.

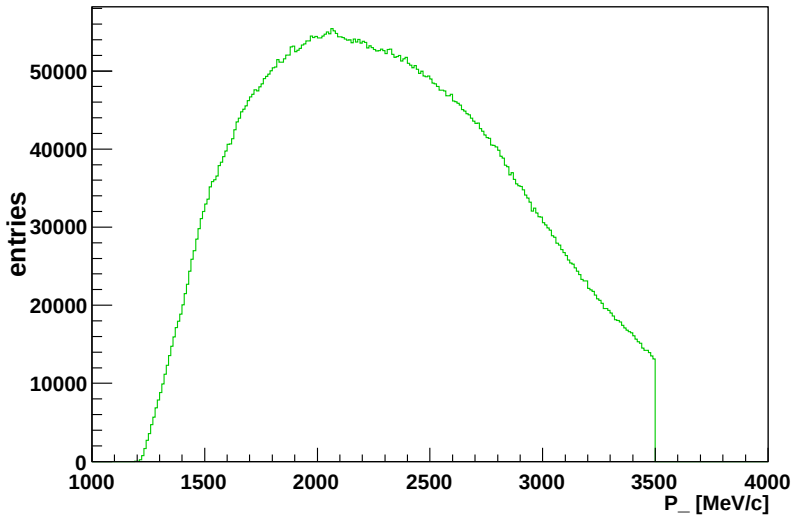

Figure 5.1: The momentum distribution of particles in negative arm. This figure shows that momenta of particles in analysed data are less or equals to 3.5GeV/c and that these particles have mostly momenta about 2-2.5GeV/c.

To study admixture of protons and antiprotons we need to reconstruct from available data the lengths of tracks(eq.(5.6)) (the length between upstream detectors and VH) and measured time of flight(eq.(5.3)). In Figure (5.3) the reconstructed lengths are shown. The lengths are about 8.5m for both arms. It agrees with the real distance of upstream detectors and VH.

In figures (5.4) and (5.5) are time histograms for positive and negative arms. In Figure (5.4) one can see two peaks. The big one corresponds to pions and the small one protons. But only one peak is visible in Figure (5.5). This big peak corresponds to π^- peak with small admixture of antiprotons. Antiproton peak is not observed, because their number is very small in comparison with total number of entries. To locate the antiprotons peak cuts of data in time and momenta are used. This problem is better described in next chapters.

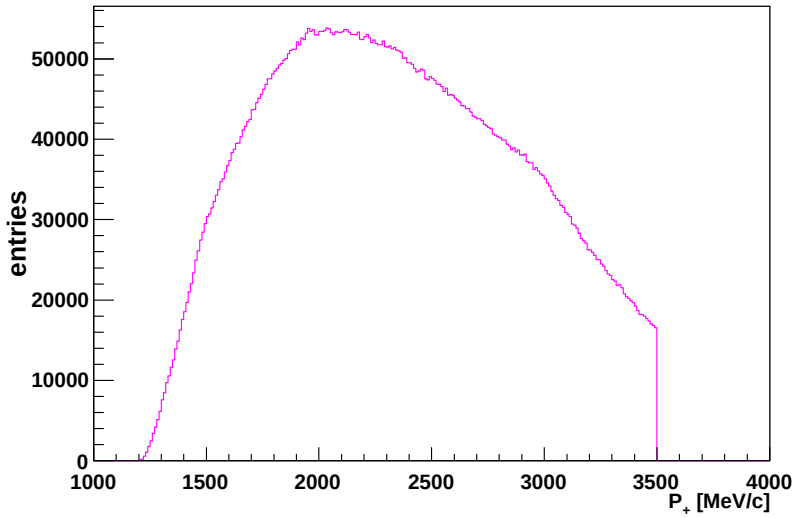

Figure 5.2: The momentum distribution of particles in positive arm. This figure shows that momenta of particles in analysed data are less or equals to 3.5GeV/c and that these particles have mostly momenta about 2-2.5GeV/c. The small protrusion on the right part of the distribution corresponds to proton admixture.

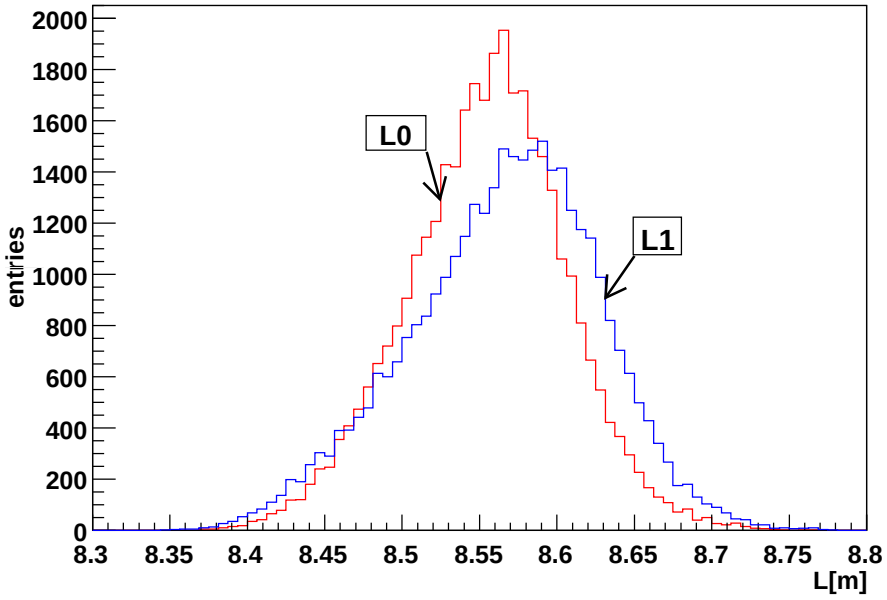

Figure 5.3: The reconstructed length of particle tracks from the target to the downstream detector (L0 - negative particles, L1 - positive particles).

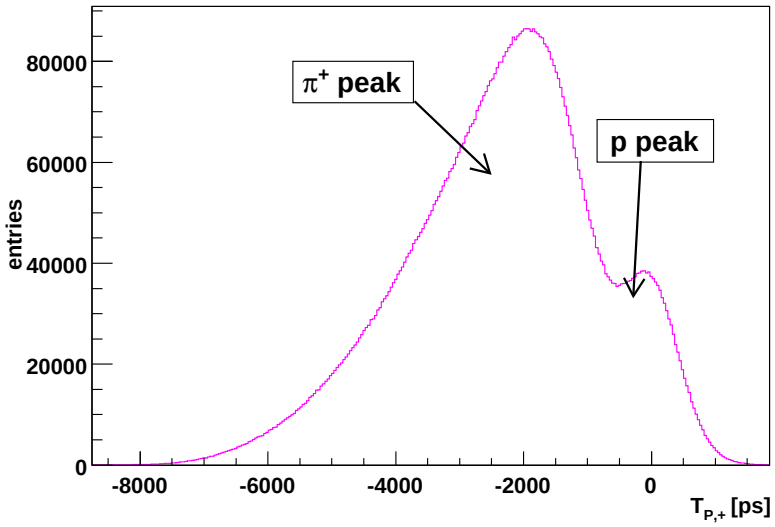

Figure 5.4: The time histogram for positive arm. On the x-axis is proton time for positive arm. Two peaks are visible in this histogram. The big one corresponds to pions and the small one corresponds to protons. The big peak is by negative x-values, because pions have bigger velocities than protons.

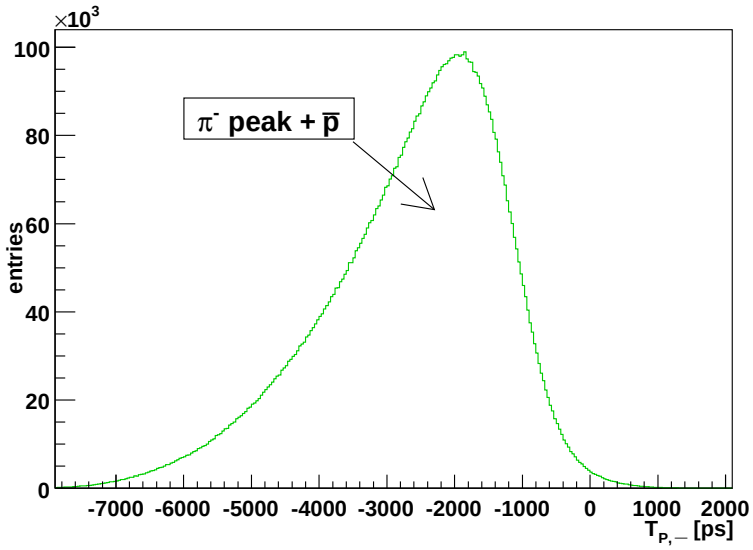

Figure 5.5: The time histogram for negative arm. One big distribution is only visible in this histogram. This distribution corresponds to π^- and antiprotons together. The antiproton peak is not separated as the proton peak in Figure (5.4), because there is very small number of antiprotons in comparison with the total number of particles in negative arm.

5.2 p and $\bar{p}$ in histograms

The next analysis refers to 2D (figures (5.6), (5.7),(5.8), (5.10)) and 3D histograms(figures (5.9), (5.11)). These histograms depend on time and momenta and show some "tails". This tail is bigger for positive arm than for negative one. The "tails" come out from a mean line. This line corresponds to π^+ in figures (5.8) and (5.10) and π^- in figures (5.6) and (5.7). Particles in the "tails" are protons in figures (5.8) and (5.10) and antiprotons in figures (5.6) and (5.7). Kaons, which also occur in aforementioned histograms, are not included in this analysis, because we suppose that they affect the (anti)proton analysis slightly. It stands to reson from these histograms that the bigger momentum the more (anti)protons blend with π^+/π^- as show lines in figures (5.6) and (5.8).

Data cuts in time and momenta, which are used for more precise analysis, were determinated from the all aforementioned figures (5.6),(5.7),(5.8),(5.10).

In figures (5.9) and (5.11) are, for comparison, 3D histograms for positive arm. The "tails" are also well visible there.

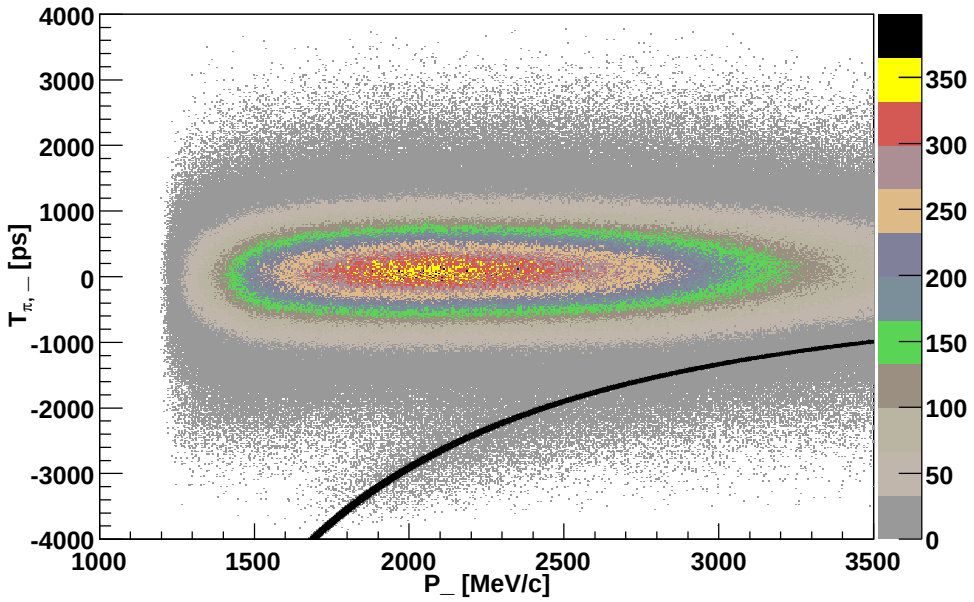

Figure 5.6: The dependence $T_{\pi,-}$ (time difference between measured time of flight and expected time of flight in case of pion in negative arm) on P_ (a momentum of negative particles). The line demonstrates behaviour of antiprotons.

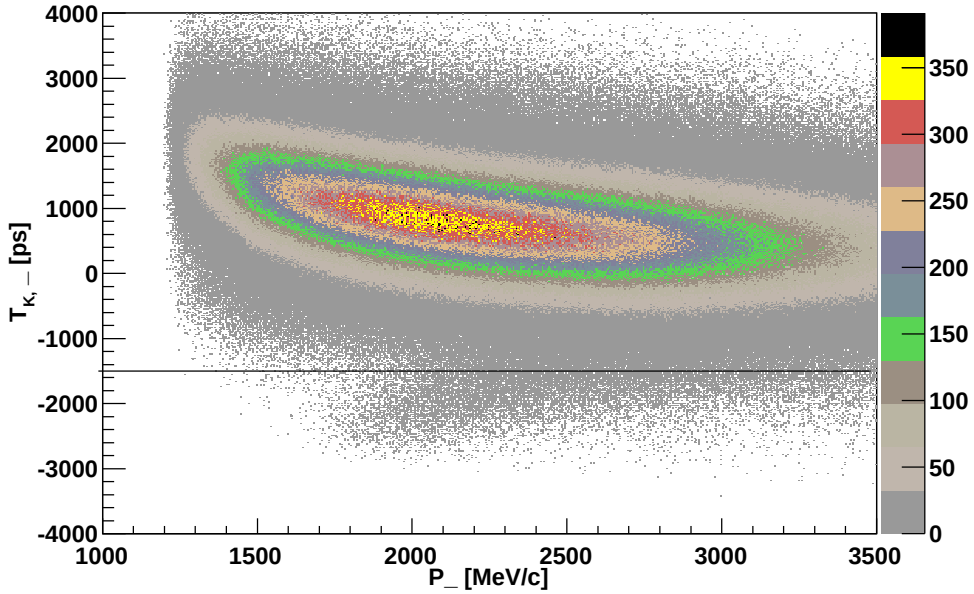

Figure 5.7: The dependence $T_{K,+}$ (time difference between measured time of flight and expected time of flight in case of kaon in negative arm) on P_- (a momentum of negative particles). The line demonstrates time cut at -1500ps.

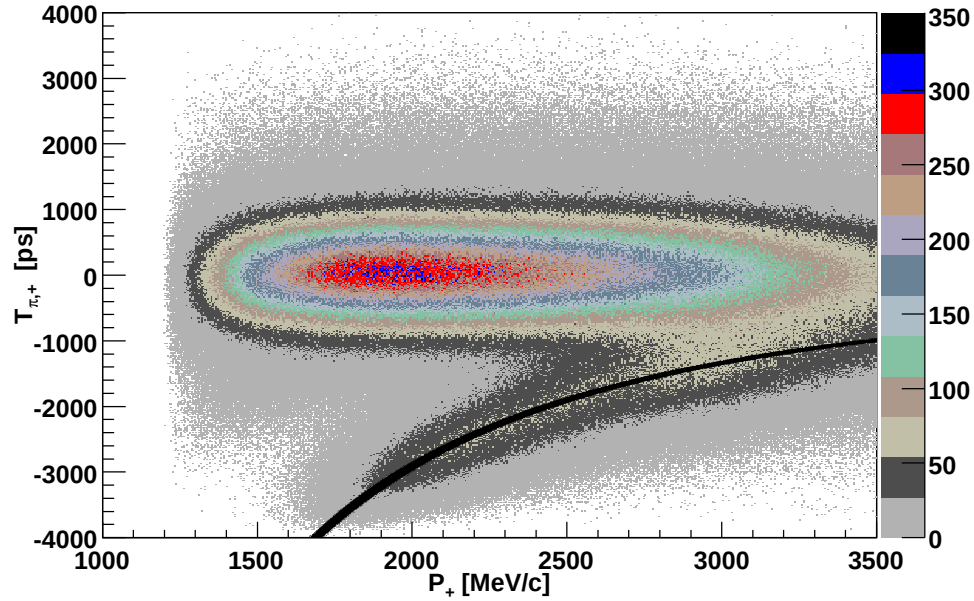

Figure 5.8: The dependence $T_{\pi,+}$ (time difference between measured time of flight and expected time of flight in case of pion in positive arm) on P_+ (a momentum of positive particles). The line demonstrates behaviour of protons.

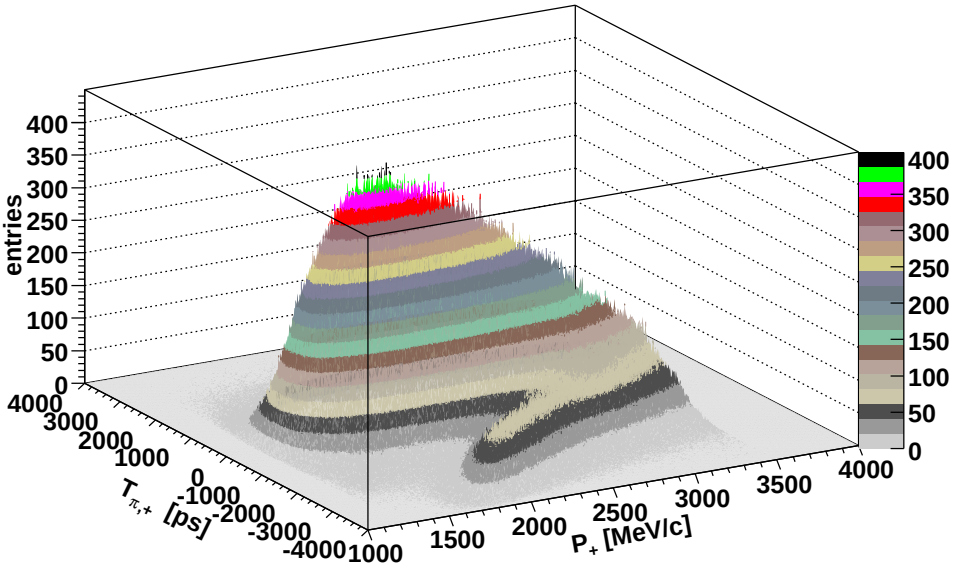

Figure 5.9: The dependence $T_{\pi,+}$ (time difference between measured time of flight and expected time of flight in case of pion in positive arm) on P_+ (a momentum of positive particles) as 3D histogram.

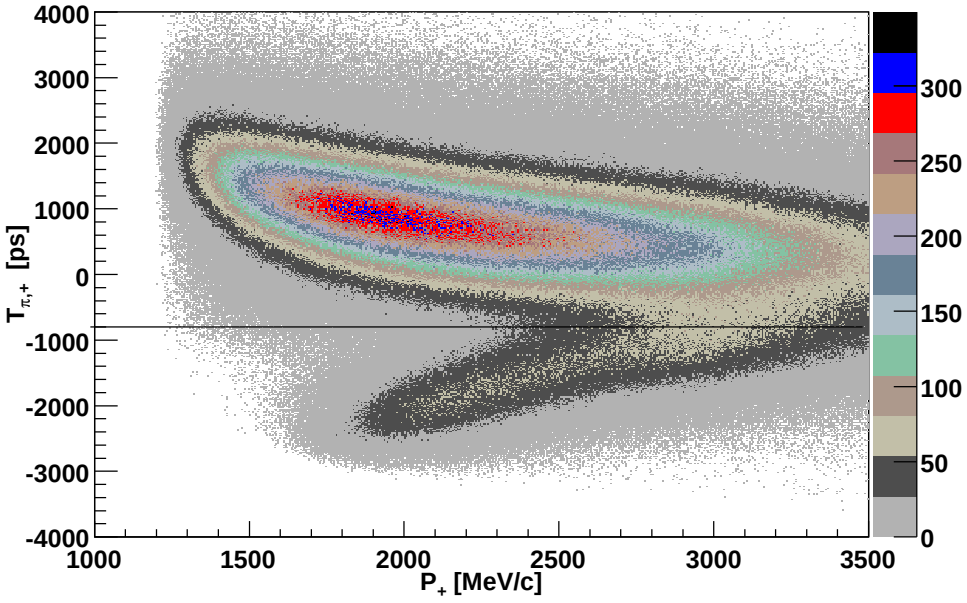

Figure 5.10: The dependence $T_{K,+}$ (time difference between measured time of flight and expected time of flight in case of kaon in positive arm) on P_+ (a momentum of positive particles). The line demonstrates time cut at -800ps.

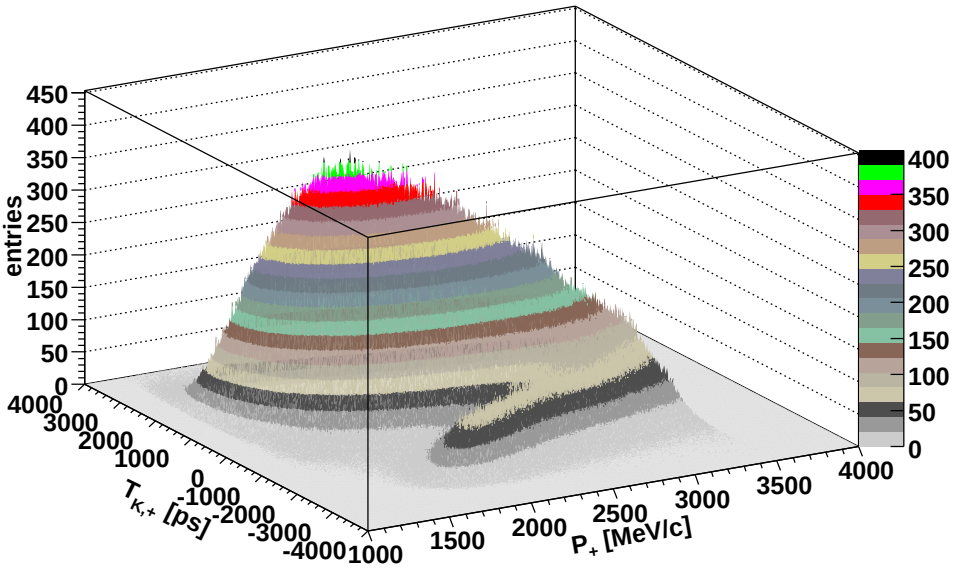

Figure 5.11: The dependence $T_{K,+}$ (time difference between measured time of flight and expected time of flight in case of kaon in positive arm) on P_+ (a momentum of positive particles) as 3D histogram.

5.3 Time resolution

For better data processing is important to find out the time resolution of detector measurement. To gain this resolution it is necessary to draw π^+ peak and π^- peak depending on T_π as show figures (5.12) and (5.13). There are cuts in time in these data to locate only π^+ and π^- to determine the best time precision value. These cuts are for π^+ peak - $T_{\pi,+} > -1500$ps and $T_{K,+} > -800$ps, for π^- peak - $T_{\pi,-} > -1800$ps and $T_{K,-} > -1500$ps. In spite of trying to make the best cuts in histograms, there is still a small admixture of protons (antiprotons) . But this admixture can be neglected and its influence on the determination of the time resolution is insignificant.

The value of the time resolution is obtained from RMS value of individual histograms. RMS equals to 574ps for positive arm and 559ps for negative arm as shown in figures (5.12) and (5.13). The time resolution value is equivalent to 0.5ns which is a satisfactory result (time of flight is about 30ns).

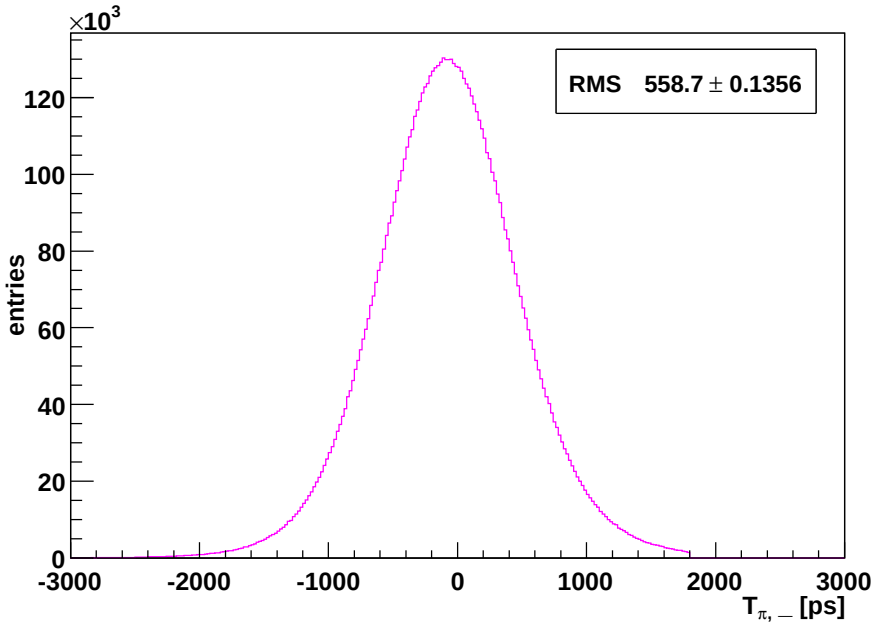

Figure 5.12: π^- peak obtained by conditions $T_{\pi,-}$ >-1800ps and $T_{K,-}$ >-1500ps. Time precision of negative arm is obtained from RMS value of this peak. RMS equals to 559ps.

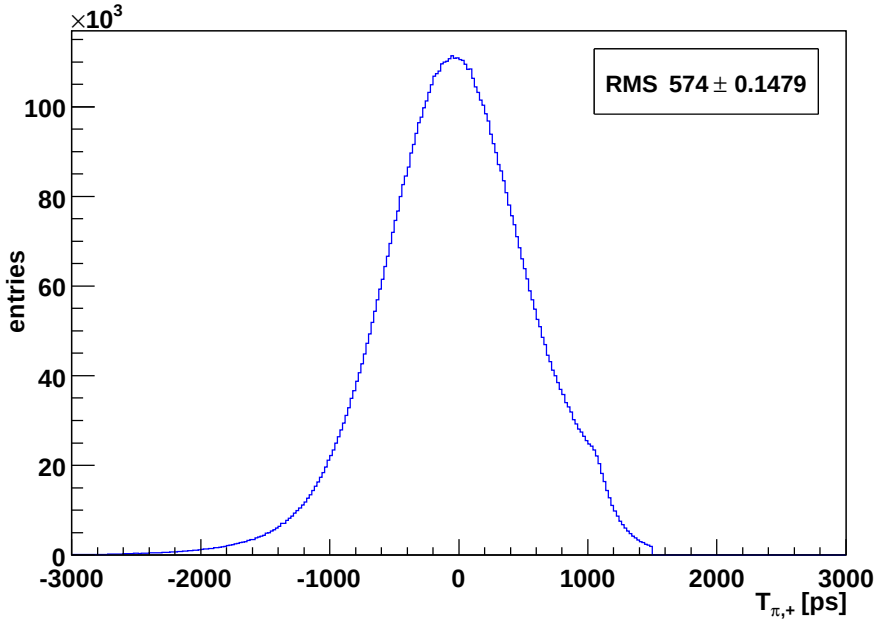

Figure 5.13: π^+ peak obtained by conditions $T_{\pi,+}$ >-1500ps and $T_{K,+}$ >-800ps. Time precision of positive arm is obtained from RMS value of this peak. RMS equals to 574ps.

Chapter 6

The analysis of p and $\bar{p}$

6.1 Total number of p

This part is devoted to estimation of the number of protons in the analysed data. The analysis is based on data separation into discrete momenta intervals. The analysis is done for each interval separately. This is due to the fact, that the difference between measured proton and pion time depends on momenta and that the total number of protons in data is very small. If the data are processed together, there are not any satisfactory results.

The data have a momentum limitation (1200,3500)MeV/c as shown (e.g.) in Figure (5.4). The width of momentum interval for proton analysis was selected 100MeV/c. Thus, there are 23 intervals in positive arm, only 19 intervals contain protons, therefore only these intervals are analysed.

Protons appear from momentum $p = 1500$MeV/c, because there is a limitation on relative momentum of pions and protons. These relative momenta have to be less or equal to 5000MeV/c.

It is necessary for each interval to draw a time histogram. The histogram in Figure (6.1) demonstrates data in momentum interval p=(1800,1900)MeV/c. There are two peaks in this figure. The big one corresponds to π^+ and the small one corresponds to protons. A mean of π^+ peak is determined by fitting by Gauss. Now the left part of π^+ peak(the green curve in Figure (6.2)) is turned in time around the mean(the yellow curve in Figure (6.2))[1].

We assumption π^+ peak symmetry and by this turning we obtain anticipated behaviour of the right part of peak. It is essential to subtract the real right part(the red curve in Figure (6.2)) from the turned part of peak to get only the protons peak(the black curve in Figure (6.2)). The results for momentum interval $p = (1800, 1900)$MeV/c is shown in Figure (6.2). This process is performed for each momentum interval separately.

There is some complication in the last four momenta intervals (p=(3100,3500)MeV/c). Proton peak intersects beyond the mean of π^+ peak in these intervals. This effect has to be taken into account. The part of proton peak beyond the mean is due to the analysis cut off and it is once again subtracted from proton peak after turning around the mean. This

[1]We do not work directly with peaks, but with individual events. We obtain pion-,proton-,antiproton- or turned peaks by processing of this events.

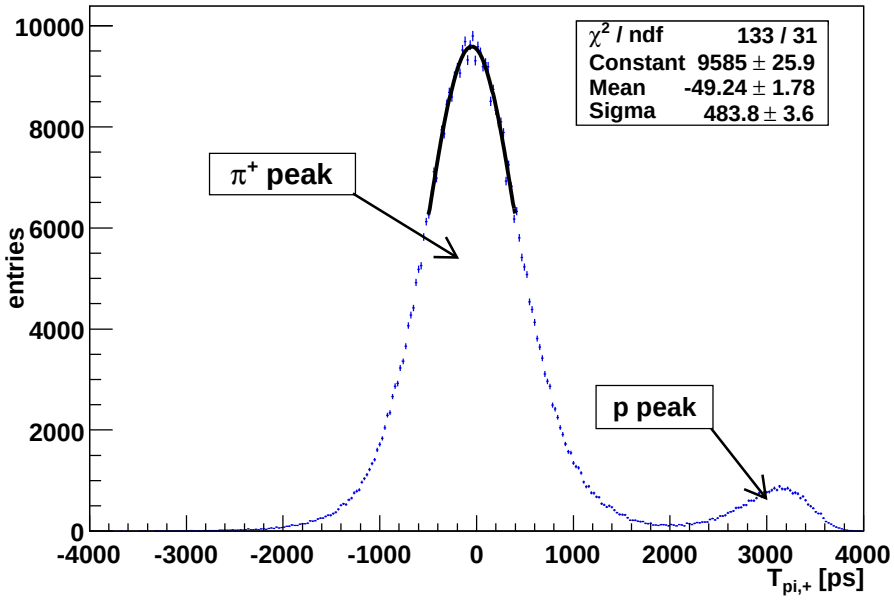

Figure 6.1: The time histogram for protons in momentum interval p=(1800,1900)MeV/c. The big peak corresponds to π^+ and the small to protons. The mean of this peak is determined by the gauss fit.

problem is shown in figures (6.4) - (6.6) for momentum interval p=(3100,3200)MeV/c. We must estimate numbers of protons beyond the mean of π^+ peak at first and than calculate correct numbers of protons in these momenta intervals.

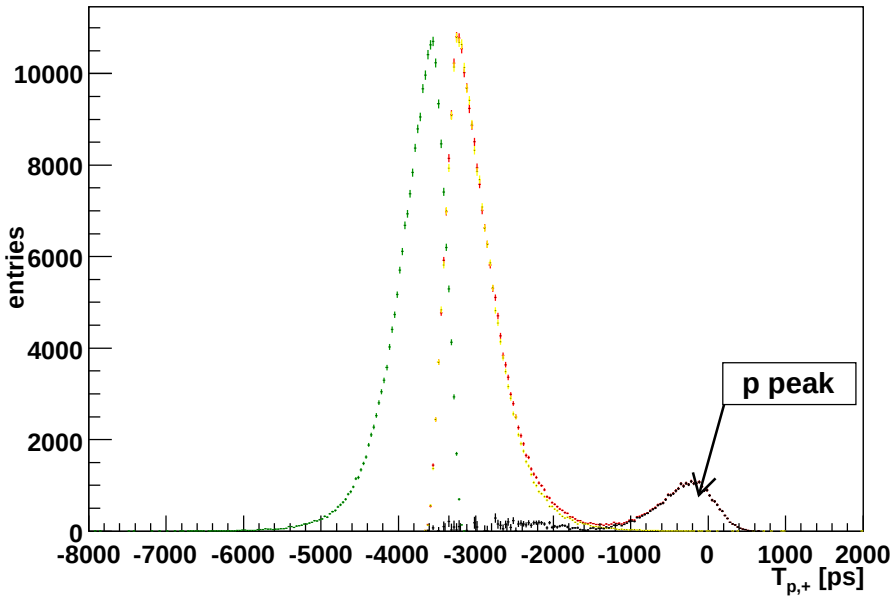

Figure 6.2: Illustration of the process for momentum interval p=(1800,1900)MeV/c. The left part(the green curve) of peak in Figure (6.1) is turned around the mean(the yellow curve) and is subtracted from the real right part of peak from Figure (6.1)(the red curve). The result is the proton peak (the black curve).

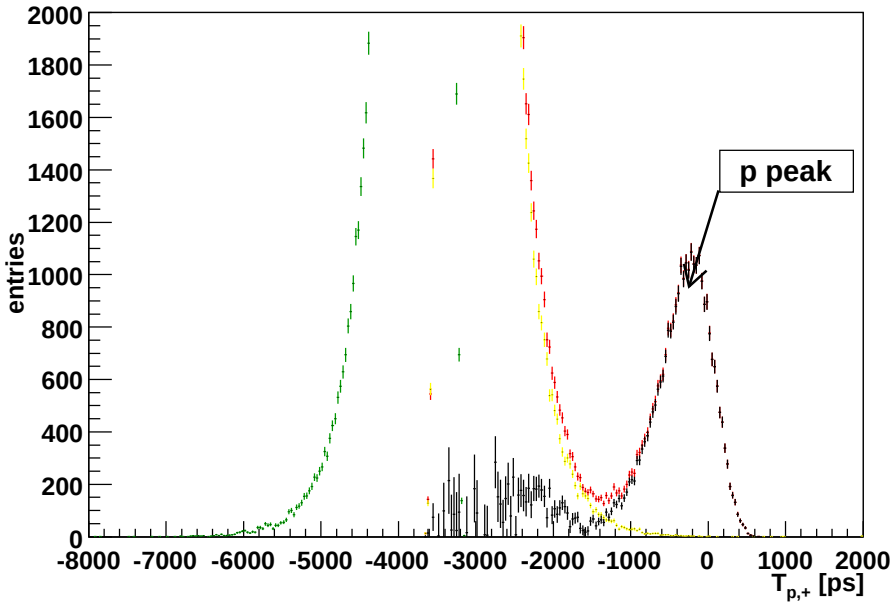

Figure 6.3: The zoom of Figure (6.2) to see better the proton peak(the black curve).

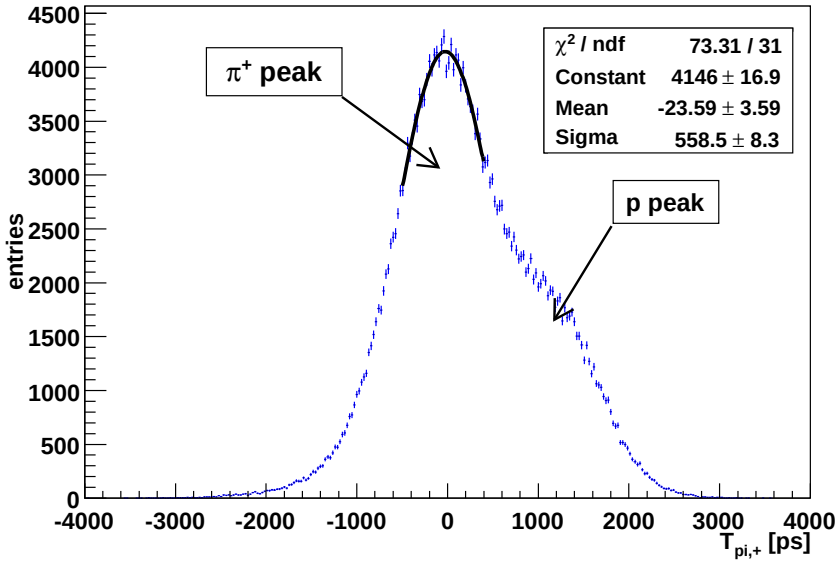

Figure 6.4: The time histogram for protons in momentum interval p=(3100,3200)MeV/c. The big peak corresponds to π^+ and the small to protons. The mean of this peak is determined by the gauss fit. Both peaks have a big overlap. This overlap has to be included in the analysis.

6.1.1 Systematic and statistic errors

Results obtained by this method are obviously burdened with errors. These errors can be separated into systematic and statistic.

Error, which arises due to the π^+ peak asymmetry, is included in systematic error. Its value is about $1,5 - 2\%$. The next source of systematic error is influence of kaons. Numbers of kaons are very small in analysed data and the error originated from their occurrance we do not impeach.

Statistic error has also two main reasons. The first source is error which is generated from determination of mean of π^+ peak by fitting with Gauss function. This error influences number of protons in individual momenta intervals as shows Table (6.1). The second one is standard statistic error which is calculated as the square root of total number of entries.

Total number of entries for standard statistic error is calculated in momenta intervals, where the π^+ peak and the proton one do not overlap, as total number of entries in the proton peak. It occurs in momentum range $p = (1600, 2000)$MeV/c. For higher momenta the π^+ and proton peaks overlap. There is a sum of entries from π^+ and proton peak taken as total number of entries.

Results for all intervals are presented in Table (6.1).

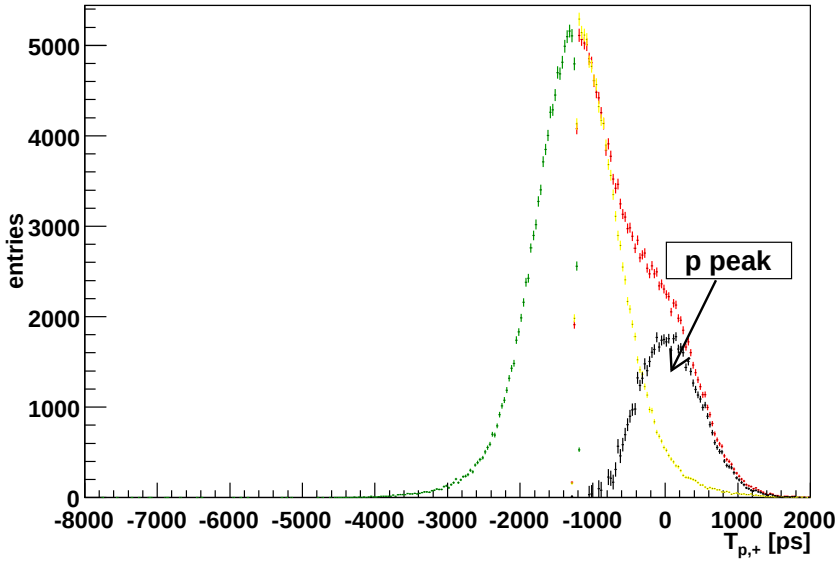

Figure 6.5: The time histogram of data in momentum interval p=(3100,3200)MeV/c. The left part(the green curve) of peak in Figure (6.1) is turned around the mean(the yellow curve) and is subtracted from the real right part of peak from Figure (6.1)(the red curve). The result is the proton peak(the black curve). The proton peak intersects beyond the mean.

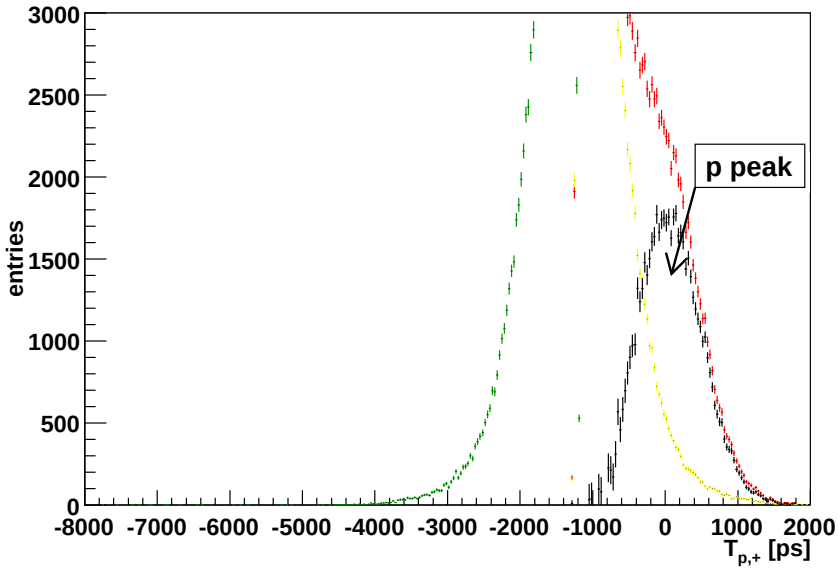

Figure 6.6: The zoom of Figure (6.5) to see better the proton peak (the black curve) and the overlapping of proton and π^+ peak.

Mom. intervals [MeV/c]	**Tot. num. of p**	**I** [%]	**II**	**III**	**IV** [%]	**V** [%]
1600-1700	2194	0.55	+3 -1	±47	+0.01 -0.01	±0.01
1700-1800	10697	2.37	+36 -18	±103	+0.03 -0.03	±0.04
1800-1900	27635	5.70	+11 -7	±166	+0.04 -0.04	±0.10
1900-2000	47001	9.20	+20 -22	±217	+0.05 -0.05	±0.16
2000-2100	59918	11.51	+34 -35	±722	+0.15 -0.15	±0.20
2100-2200	67220	12.85	+70 -62	±723	+0.15 -0.15	±0.22
2200-2300	70713	13.66	+123 -145	±720	+0.16 -0.17	±0.24
2300-2400	71882	14.20	+786 -738	±711	+0.30 -0.29	±0.25
2400-2500	72122	14.91	+595 -692	±695	+0.27 -0.29	±0.26
2500-2600	69655	15.04	+664 -640	±681	+0.29 -0.29	±0.26
2600-2700	70759	16.12	+771 -782	±663	+0.33 -0.33	±0.28
2700-2800	71240	17.17	+856 -954	±644	+0.36 -0.39	±0.30
2800-2900	72845	18.64	+1053 -1020	±625	+0.43 -0.42	±0.33
2900-3000	73231	19.94	+845 -847	±606	+0.40 -0.40	±0.35
3000-3100	66580	20.24	+954 -949	±573	+0.46 -0.46	±0.35
3100-3200	59574	20.28	+1040 -1053	±534	+0.55 -0.56	±0.35
3200-3300	48193	19.08	+936 -906	±496	+0.58 -0.57	±0.33
3300-3400	41257	18.60	+958 -1002	±459	+0.67 -0.69	±0.33
3400-3500	33844	17.09	+916 -1004	±419	+0.76 -0.81	±0.30

I...percents of p from all particles of appropriate interval
II...affecting of number of protons in individual momenta intervals by the mean error
III...standard statistic error
IV...total statistic error
V...total systematic error

Table 6.1: The total number of protons in individual momenta intervals.

6.2 Total number of $\bar{p}$

The same procedure for finding antiprotons in negative arm is applied. The width of momentum interval was selected 200MeV/c. The data have the same momentum limitation (1200,3500)MeV/c as for protons (Figure (5.5)) thus, there are about 11 intervals in negative arm.

Antiprotons appear from momentum $p = 1600$MeV/c, because there is a limitation on relative momentum of pions and antiprotons (these relative momentum has to be less or equal to 4500MeV/c). All parts, where antiprotons appear, have width of 200MeV/c, only the last one has 300MeV/c.

The analysis is slightly complicated, as was several times mentioned, due to the fact that the number of antiprotons is much smaller than number of protons. Cuts in time are therefore determined to separate overflowing large number of π^-.

The time cuts are defined in each part separately, because the higher momenta, the more antiprotons are connected to π^- as one can see in Figure (5.8).

The effect which appears by protons - the proton peak intersects beyond the mean of π^+ peak in large momenta - we do not contemplate.

The illustration of analysis for momentum interval $p = (2000, 2200)$MeV/c is shown in figures (6.8) and (6.9). To select the zone, where antiprotons are located in this interval, the cut $T_{\pi,-} < -1690$ps is used ($T_{\pi,-}$ - time difference between measured time of flight and expected time of flight in case of pion between Vertical hodoscope and upstream detectors for negative arm). Now the value of this cut is turned around the mean of π^- peak (to find out the mean of π^- peak the Gauss function is used as for the analysis of protons) and the part whose time is bigger than the inverse value, is selected(the blue curve). This cut off part of π^- peak is then turned back about the mean(the green curve). This step is important for obtaining anticipated behaviour of π^- peak in real right part(the violet curve) - the part, where antiprotons are located.

In Figure (6.8) one can see that the real right part(the violet curve) and left part(the green curve) of the peak are not identical. This difference is taken as the asymmetry. Asymmetries for all momenta intervals are mentioned in Table (6.2). To obtain correct numbers of antiprotons it is important to make these peaks maximal equable (i.e. the left part must be adapt to the right one. The right part must not be change, because there are antiprotons in this part).

To get number of antiprotons similar procedure as for protons is made. The real right part(the violet curve) is subtracted from the turned part(the green curve) which is modify to the asymmetry and some small peak (the black curve) - antiprotons peak is obtained. The resulting peak is not ideal and symmetrical but for the analysis is satisfying.

Illustration of the same process for momentum interval p=(2800,3000)MeV/c is shown in figures (6.10) and (6.11) (where time cut is $T_{\pi,-} < -662$ps). Results for all intervals are mentioned in Table (6.2).

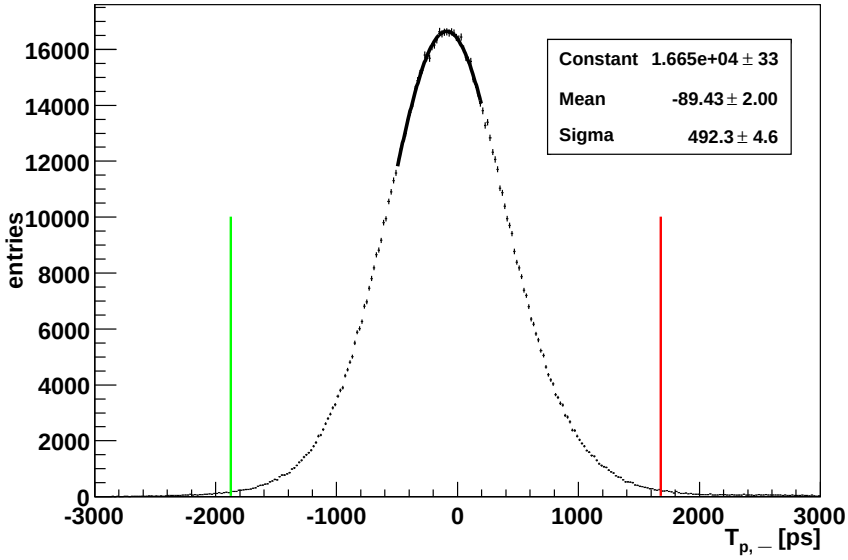

Figure 6.7: The distribution of π^- peak with an admixture of antiprotons in momentum interval p=(2000,2200)MeV/c. The peak is fitted by Gauss to find out the mean. The red line means the time cut to separate the zone, where antiprotons are located. The green line means the inverse value of the time cut. According to this the anticipated behaviour of π^- peak in the zone, where antiprotons are located, is obtained.

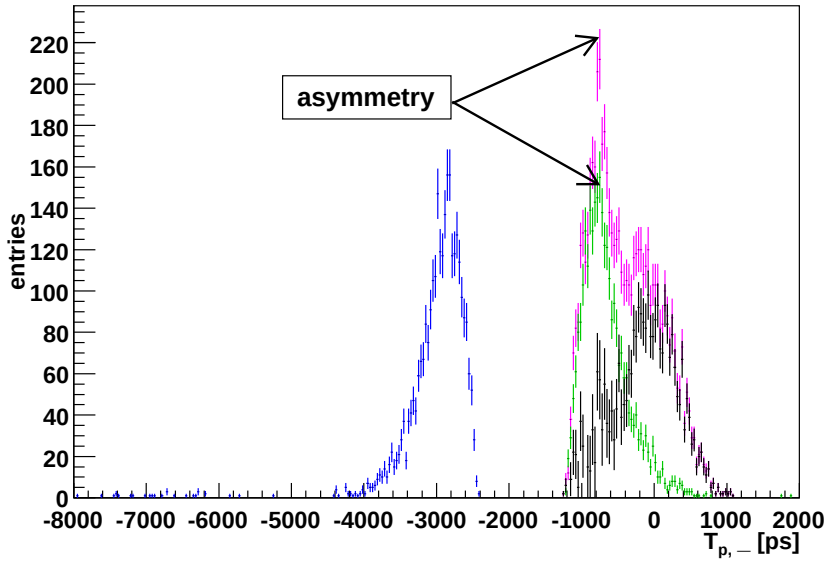

Figure 6.8: The peak asymmetry for momentum interval p=(2000,2200)MeV/c. As one can see the cut right(the violet color) and the left part(the green color) of the peak are not identical. This difference is taken as the asymmetry. The asymmetry for this peak is 14% and it belongs to the biggest in the analysis.

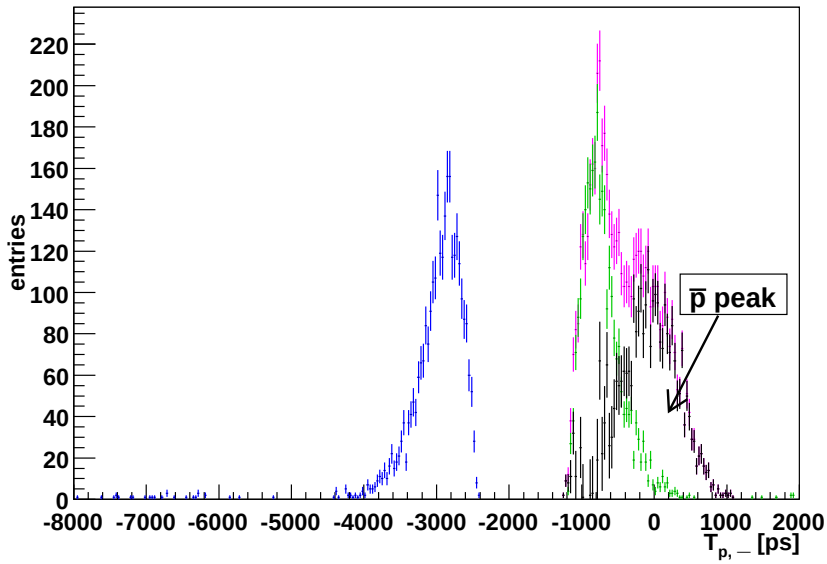

Figure 6.9: Antiproton peak for momentum interval p=(2000,2200)MeV/c. In this histogram the time cut is $T_{\pi,-} < -1690$ps ($T_{\pi,-}$ - time difference between measured time of flight and expected time of flight in case of pion between Vertical hodoscope and upstream detectors for negative arm). The cut left part(the blue curve) is turned about the mean(the green curve), modify to the asymmetry and subtracted from the cut right part(the violet curve). The result is the antiproton peak(the black curve).

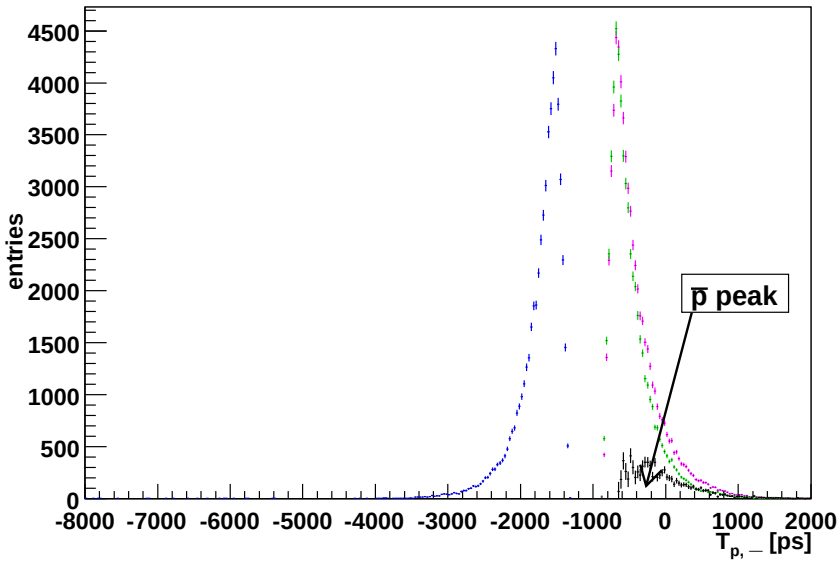

Figure 6.10: Antiproton peak with number of entries for momentum interval p=(2800,3000)MeV/c. In this histogram the time cut is $T_{\pi,-} < -662$ps. The cut left part (the blue curve) is turned about the mean(the green curve), modify to the asymmetry and subtracted from the cut right part(the violet curve). The result is the antiproton peak(the black curve).

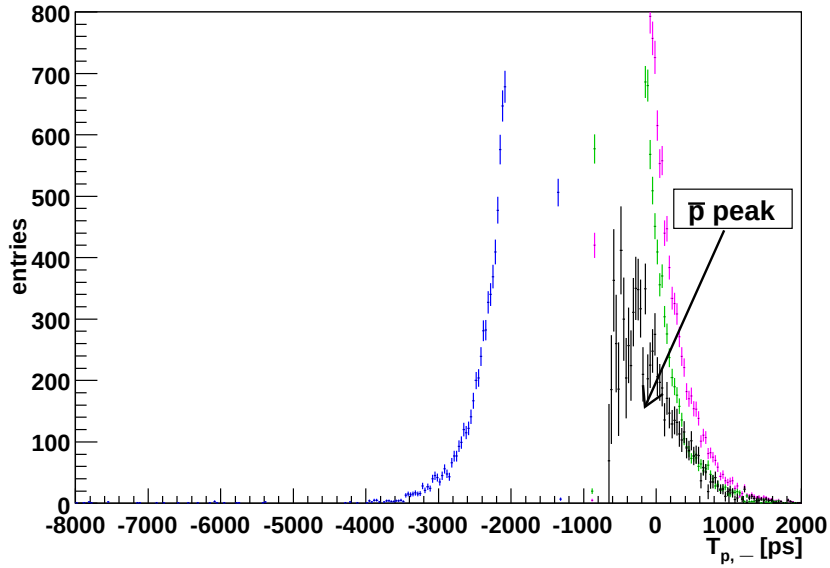

Figure 6.11: The zoom of Figure (6.10) to see better the antiproton peak(the black curve).

6.2.1 Systematic and statistic errors

Results of antiprotons have as results of protons two kind of errors - systematic and statistic errors.

The process of determination of these errors is the same as for protons (see part 6.1.1). But with a difference that in momentum interval $p = (2000, 3500)$MeV/c, where the π^- peak and the antiproton one overlap, is a sum of entries from cut right part(the violet color) of the peak (e.g. in Figure (6.9)) and cut left part(the green color) of the peak (e.g. in Figure (6.9)) taken as total number of entries for standard statistic error.

Thoroughly described process is done for each momentum interval separately. All results are visible in Table (6.2).

Momenta intervals [MeV/c]	**Tot. num. of $\bar{p}$**	**I[%]**	**II**	**Asymmetry [%]**	**III**
1600-1800	43	0.005	+1 -0	0	±7
1800-2000	1140	0.11	+1 -1	0	±34
2000-2200	2776	0.26	+19 -11	14	±92
2200-2400	4475	0.43	+56 -69	16	±141
2400-2600	6003	0.61	+155 -141	11	±193
2600-2800	5962	0.69	+119 -220	7	±254
2800-3000	8635	1.23	+321 -695	3	±342
3000-3200	6059	1.13	+842 -839	1	±393
3200-3500	5621	1.07	+1248 -1188	0	±341

I... percents of $\bar{p}$ from all particles of appropriate interval
II... affecting of number of antiprotons in individual momenta intervals by the mean error
III... standard statistic error

Table 6.2: The total number of antiprotons in individual momenta intervals.

Chapter 7

The second data

It was necessary for final analysis to work with different data, because we can not calculate from the first data Δt_P (a difference between outgoing time from the target for positive and negative particle in case those particles are proton and antiproton) which is very important for the next analysis.

The number of the new data is about two times larger than previous data. These second data also include the old ones (the old ones thus form about a half of the new ones.).

The variables that are disposable and are used, are :

- measured times in Scintillation fibre detector, Ionization Hodoscope and Vertical Hodoscope,
- particles momenta in negative and positive arm.

Scintillation fibre detector and Ionization Hodoscope are close together. It is useful their times average to one common time. For calculating this time it is necessary to know time resolution of each plane of these upstream detectors. Scintillation fibre detector had two planes and Ionization Hodoscope had four planes in 2001 when the date were collected.

RMS value and mean of pion peak are determined for each plane for negative arm. The time resolutions of individual planes are determined from RMS values. The time resolutions are needed for calculating the "new" time and mean value for optimalisation this result.

Only the negative arm is analysed because admixture of antiprotons in negative arm is much lower than protons in positive arm and admixture of K^- is also less than of K^+. To select just the pion peak, momenta of particles in negative arm have to be less than 2GeV/c.

It is needed to select reasonable range for RMS calculation. We determine RMS in the range $\pm$4RMS. Results are mentioned in Table (7.1). It is evident from this table that time resolutions of individual planes are about 700-800ps. When the time resolutions are known, the "new" time is calculated as weighted average outspreads to the fourth plane of Ionization hodoscope.

Detector	Plane	RMS	Mean
Scifi	I	811.07	197.71
	II	828.49	175.81
IH	I	763.58	35.41
	II	1077.17	36.48
	III	7719.99	-31.61
	IV	731.24	-20.95

Table 7.1: The time resolution and mean value for each plane of upstream detectors (Scifi - Scintillation fibre detector and IH - Ionization hodoscope) for negative arm.

$$\overline{x} = \frac{\sum \frac{x_i}{\sigma_i^2}}{\sum \frac{1}{\sigma_i^2}} \tag{7.1}$$

where $\overline{x}$ is the "new" time, x_i the measured time in some plane which is offset to correspond to the fourth plane of IH and σ_i is RMS value of the same plane.

The recalculated time compared with measured time in fourth plane in Ionization hodoscope is shown in Figures (7.1). It is perceptible that the measured time became better thank to the recalculation. The peak which responds to recalculated time is narrower (⇒higher) than the peak which corresponds to the measured times.

We now establish new variables:

- $\mathrm{T}_{\pi/P,-/+}$, *time difference between expected and measured time of flight in case of pion or kaon between Vertical Hodoscope and recalculated time from upstream detectors (Scintillation fibre detector and Ionization hodoscope) to the fourth plane in Ionization hodoscope. The first index means the kind of particle (π-pion and P-proton) and the second one means the charge (− negative and + positive).*

- Δt_π, *a difference between outgoing time from the target for positive and negative particle in case those particles are π^+ and π^-.*

- Δt_P, *a difference between outgoing time from the target for positive and negative particle in case those particles are proton and antiproton.*

- $\mathrm{P}_{-/+}$, *a momentum of − negative or + positive particle.*

The distribution of Δt_π is shown in Figure (7.2). To know right distribution of Δt_P it is necessary to use some limitations in time and momenta as Figure (7.3) shows.

Without any time limitations the distribution of Δt_P (e.g. in momentum interval p=(2200,2400)MeV/c) looks quaintly Figure (7.4) in comparison with Figure (7.3).

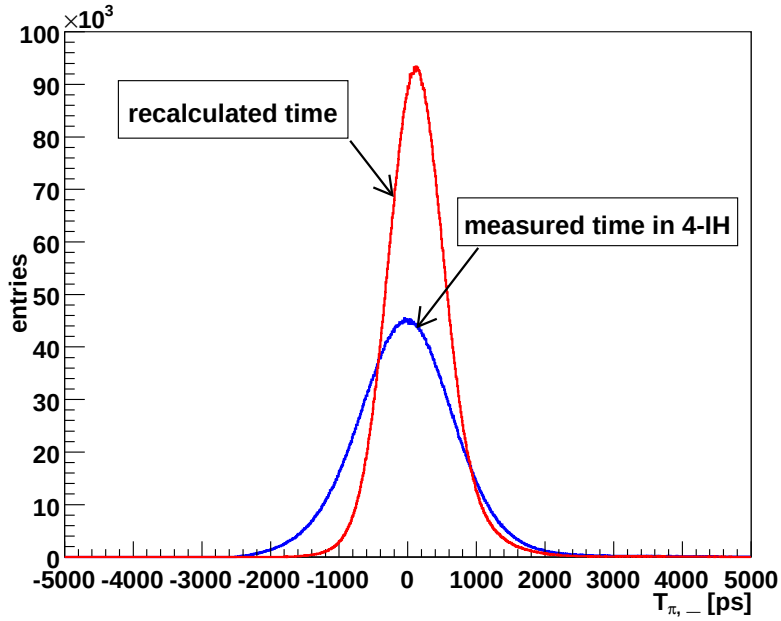

Figure 7.1: Comparison of the recalculated time to the fourth plane of Ionization hodoscope and the measured time in this fourth plane. It is perceptible that the peak which corresponds to recalculated time (the red curve) is narrower ($\Rightarrow$ higher) than the peak which responds to the measured time (the blue curve). This implies that the recalculated time is better.

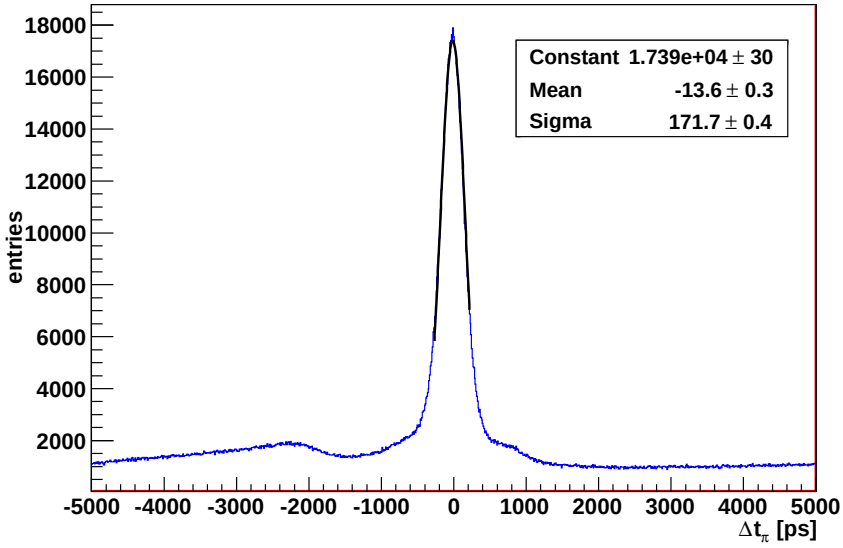

Figure 7.2: The distribution of Δt_π (a difference between outgoing time from the target for positive and negative particles in case those particles are π^+ and π^-) with gauss fit to find out its RMS value.

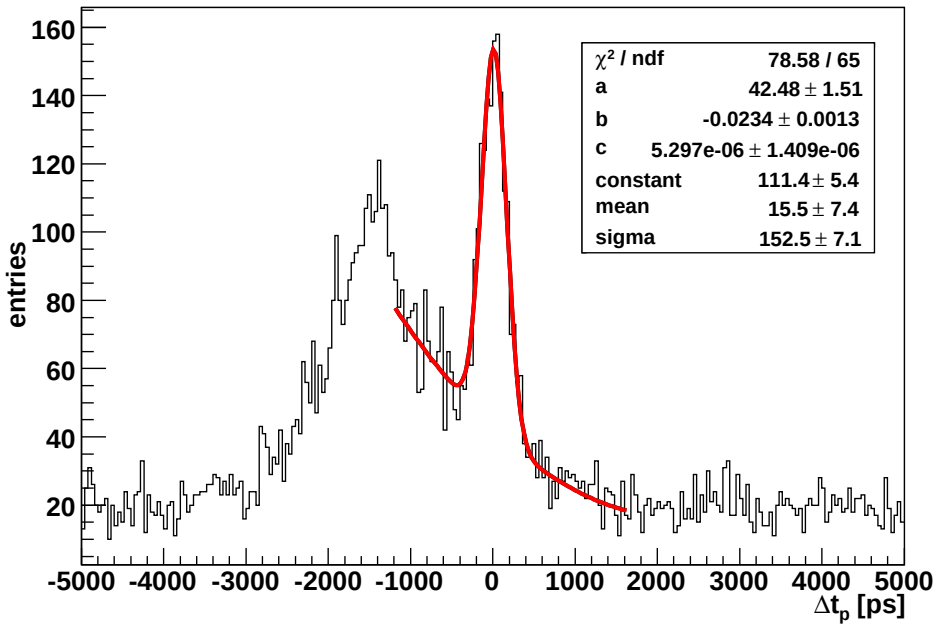

Figure 7.3: The distribution of Δt_P (a difference between outgoing time from the target for positive and negative particle in case that particles are proton and antiproton) on background of Δt_π with conditions that momenta of particles are less than 2GeV/c and proton time of first plane in SciFi for both tracks is greater than -200ps to select a lot of $p\bar{p}$ pairs at the expense of $\pi^+\pi^-$ pairs. The distribution is fitted by gauss and quadratic multinominal to find out RMS value of Δt_P.

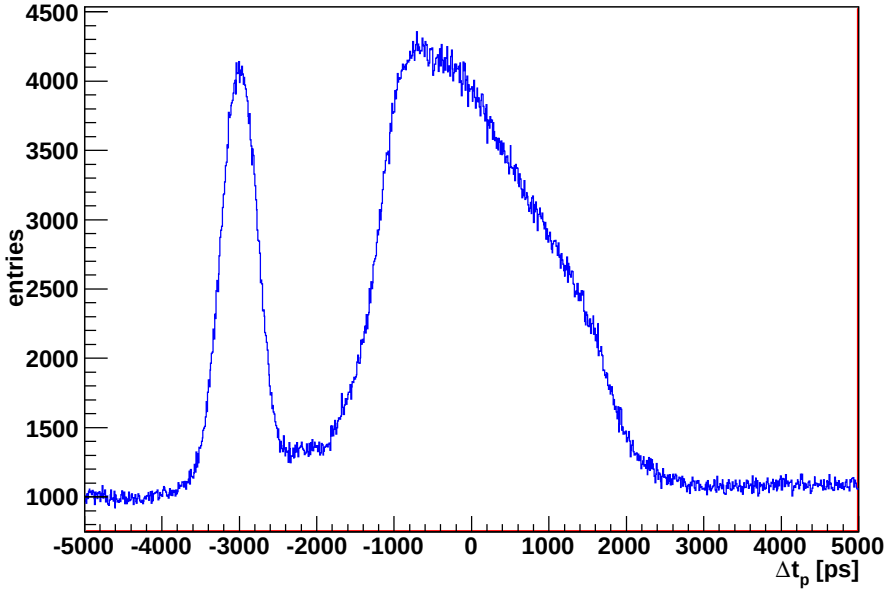

Figure 7.4: The distribution of Δt_P (a difference between outgoing time from the target for positive and negative particle in case those particles are proton and antiproton) in momentum interval p=(2200,2400)MeV/c without any time cuts. The big wide peak agrees with $p\bar{p}$ pairs with an admixture of $\pi^+\bar{p}$ pairs, $\pi^- p$ pairs and $\pi^-\pi^+$ pairs due to any time limitations.

Chapter 8

The analysis of $p\bar{p}$ pairs

8.1 Total number of $p\bar{p}$ pairs

A process to obtain total number of $p\bar{p}$ pairs in new data is described in this part. The momentum interval for this analysis was selected $p = (1600, 2600)$MeV/c. It is not possible to analyse higher momenta, because for these momenta the proton and antiproton peaks have very large overlap with π^+ and π^- peaks as one can see in figures (5.6), (5.7), (5.8) and (5.10). Our analysis of these momenta would not get good results. The momentum interval, where we make the analyse ($p = (1600, 2600)$MeV/c) was divided in 5 intervals with a width 200MeV/c.

2dimensional histograms of dependence $T_{P,-}$ and $T_{P,+}$ are drawn to find out numbers of $p\bar{p}$ pairs.

Such histogram is shown in Figure (8.1). Four various zones are located here. The small upper right corresponds to $p\bar{p}$ pairs. The others are from the smallest till the largest $\pi^- p$ pairs, $\pi^+\bar{p}$ pairs and $\pi^-\pi^+$ pairs.

To select only right[2] $p\bar{p}$ pairs it is essential to apply some condition. Condition $|\Delta t_\pi|$ <500ps is used to determine an admixture of right $p\bar{p}$ pairs in right $\pi^-\pi^+$ pairs and condition $|\Delta t_P|$ <500ps is used to determine number of right $p\bar{p}$ pairs in all data.

The value of condition 500ps is used for the reason that it is value which is used for standard analysis of right $\pi^-\pi^+$ pairs. The statistic decreases and a form of the distribution transforms slightly after this requirement as it is apparent from figures (8.2), (8.3), (8.4).

Next step is selecting the area where $p\bar{p}$ pairs are located with the help of time cuts. These time cuts are different for each momenta intervals as it is shown in Table (8.1).

Projection onto x-axis is made with consistent time cut in positive arm (e.g. Figure (8.5)). One can see a small peak - $p\bar{p}$ pairs peak. The number of these pairs in individual momenta intervals is found out with the help of time cut in negative arm and integral of arisen distribution. This procedure is made for each momentum interval and limitation of Δt_π or Δt_P separately. All results are published in Table (8.1).

[2]Right pairs are pairs which origin from the same proton nuclei collisions.

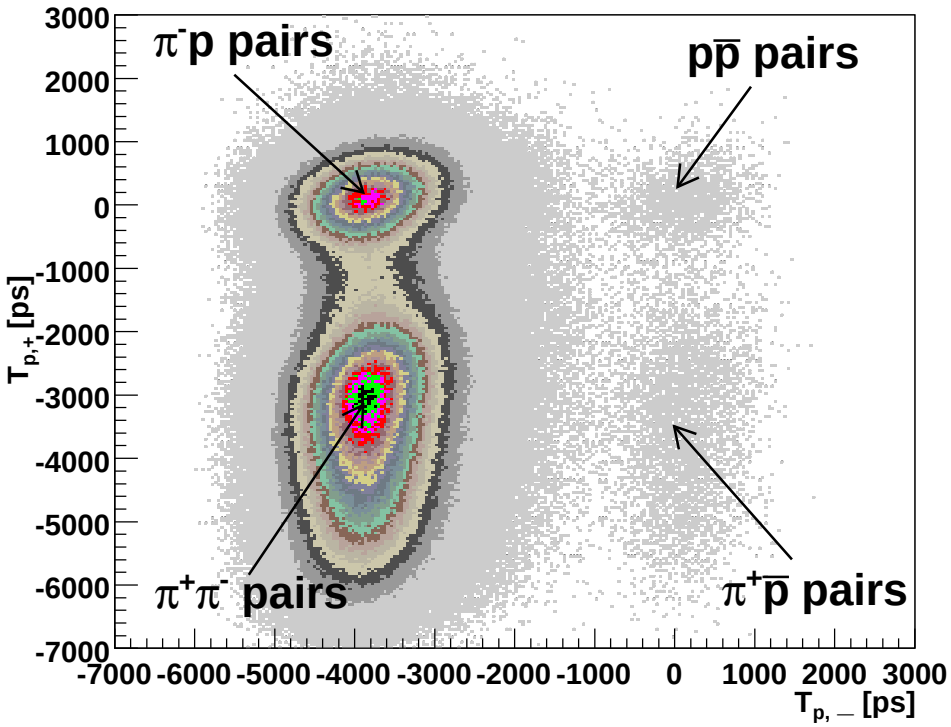

Figure 8.1: Distribution of dependence $T_{P,-}$ (time difference between measured time of flight and expected time of flight in case of proton between Vertical Hodoscope and upstream detectors for negative arm) and $T_{P,+}$ (time difference between measured time of flight and expected time of flight in case of proton between Vertical Hodoscope and upstream detectors for positive arm) for momentum interval p=(1600,1800)MeV/c with four zones corresponding to different particles pairs.

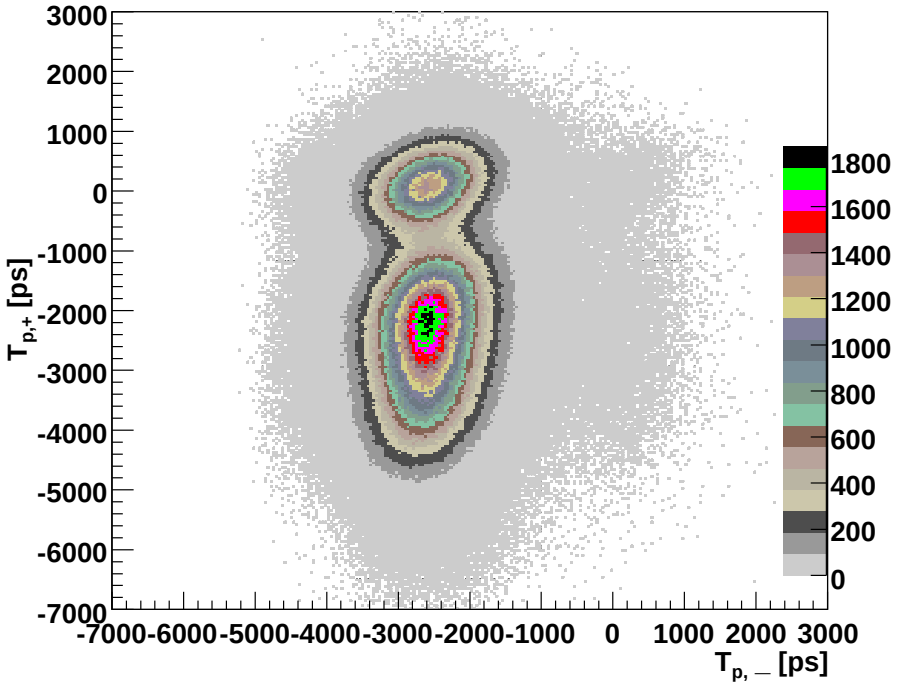

Figure 8.2: Distribution of dependence $T_{P,-}$ (time difference between measured time of flight and expected time of flight in case of proton between Vertical Hodoscope and upstream detectors for negative arm) and $T_{P,+}$ (time difference between measured time of flight and expected time of flight in case of proton between Vertical Hodoscope and upstream detectors for positive arm) for momentum interval p=(2000,2200)MeV/c without any limitations to Δt_π or Δt_P.

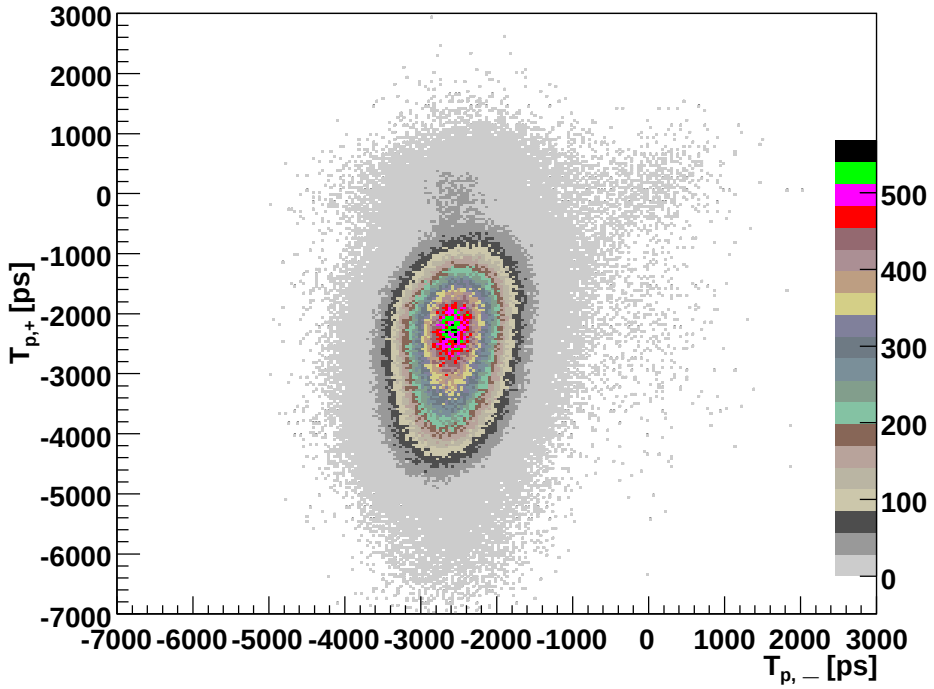

Figure 8.3: Distribution of dependence $T_{P,-}$ (time difference between measured time of flight and expected time of flight in case of proton between Vertical Hodoscope and upstream detectors for negative arm) and $T_{P,+}$ (time difference between measured time of flight and expected time of flight in case of proton between Vertical Hodoscope and upstream detectors for positive arm) for momentum interval p=(2000,2200)MeV/c with condition $|\Delta t_\pi|$ <500ps.

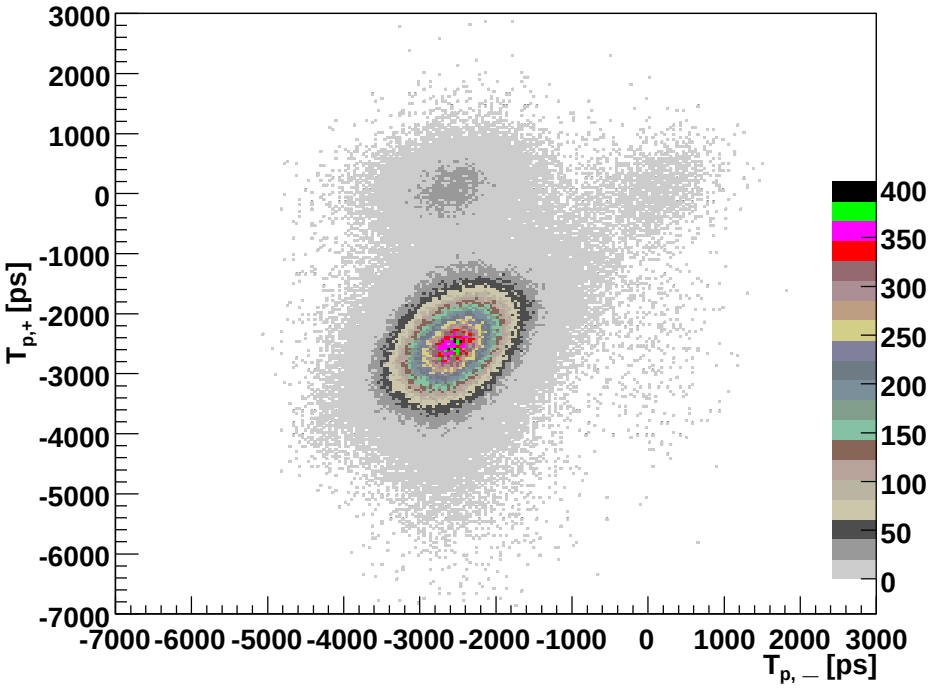

Figure 8.4: Distribution of dependence $T_{P,-}$ (time difference between measured time of flight and expected time of flight in case of proton between Vertical Hodoscope and upstream detectors for negative arm) and $T_{P,+}$ (time difference between measured time of flight and expected time of flight in case of proton between Vertical Hodoscope and upstream detectors for positive arm) for momentum interval p=(2000,2200)MeV/c with condition $|\Delta t_P|$ <500ps.

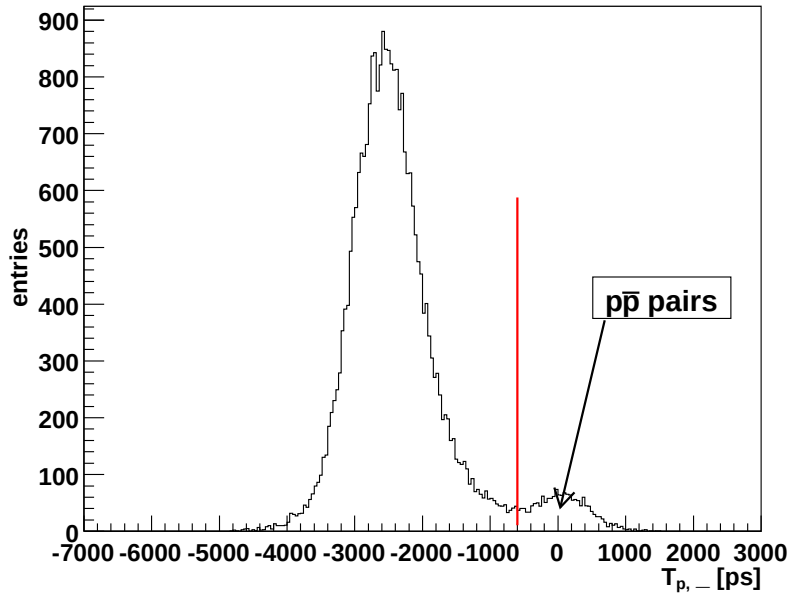

Figure 8.5: Projection onto x-axis with time cut $T_{P,+}$>-1000 and limitation on $|\Delta t_P|$<500ps (Δt_P...a difference between outgoing time from the target for positive and negative particle in case that particles are proton and antiproton) for momentum interval p=(2000,2200)MeV/c. The small peak corresponds to $p\bar{p}$ pairs. The red line means the time cut in negative arm ($T_{p,-}$= -600ps).

momentum interval [MeV/c]	**cut1 [ps]**	**cut2 [ps]**	**entries1**	**entries2**	**A [%]**
1600-1800	-1000	-1000	258	780	0.02
1800-2000	-800	-1000	427	1191	0.03
2000-2200	-600	-1000	859	1706	0.04
2200-2400	-600	-800	1461	2261	0.05
2400-2600	-500	-800	2603	3383	0.09

cut1...time limitation in negative arm
cut2...time limitation in positive arm
entries1...number of $p\bar{p}$ pairs with condition $|\Delta t_\pi|$ <500ps
entries2...number of $p\bar{p}$ pairs with condition $|\Delta t_P|$ <500ps
A...percents of $p\bar{p}$ pairs in all pairs of appropriate interval

Table 8.1: Total number of $p\bar{p}$ pairs in individual momenta intervals.

8.1.1 Systematic and statistic errors

Systematic errors in this analysis rise from time cuts in 2D histograms. Cuts in $T_{P,+}$ evoke that some protons are cut off and some π^+ are added, cut in $T_{P,-}$ evoke that some antiprotons are cut off and some π^- are added. Percentage of rates are determined

from analysis of 1dimensional histograms for positive and negative arm with momentum intervals within the range 200MeV/c which is the same as momentum interval for 2D histograms.

This calculation is made by using the old data. We suppose that percentage substitution of particles is consistent for the first and the second data. The errors can not be calculated for the first momentum interval p=(1600,1800)MeV/c, because the number of antiprotons in this interval in "old" data is very small (almost negligeable).

This procedure of finding systematic error is the same as for finding numbers of protons and antiprotons which is mentioned in parts 6.1 and 6.2. Percents of cut off protons or antiprotons and percents of added π^+ or π^- are calculated according to the corresponding time cuts which were used for determination of number of $p\bar{p}$ pairs. An illustration of this method for momentum interval p=(2000,2200)MeV/c for positive and negative arm is shown in figures (8.6) and (8.7).

In Figure (8.6) is an illustration of calculating of the number of added π^+ and cut off p. The number of added π^+ is calculated from the whole part of π^+ peak(the yellow curve) which occurs above the corresponding time cut(the blue line). The number of cut off protons is calculated only from the small part of proton peak(the black curve) which occurs below the corresponding time cut. The remaining part of the black curve does not relate to protons. It includes π^+ peak asymmetry and some admixture of K^+ as it was earlier mentioned.

In Figure (8.7) one can see an illustration of calculating of the number of added π^- and cut off $\bar{p}$. The number of added π^- is calculated from part of π^- peak(the green curve) which occurs above the corresponding time cut(the blue curve) and the number of cut off $\bar{p}$ is calculated from part of $\bar{p}$ peak(the black curve) which occurs below the corresponding time cut(the blue curve).

These results are recalculated to correspondent percents of cut off $p\bar{p}$ pairs and percents of added other pairs (as $\pi^- p$ pairs, $\pi^+\bar{p}$ pairs or $\pi^+\pi^-$ pairs). It is made on the assumption that the production of positive and negative particle is independent (it is not truth but it may take in this way in first approximation). For calculation is applied probability formula for independent events[3]. Statistic error is taken as the square root of total number of $p\bar{p}$ pairs in individual momenta intervals. Results are presented in Table (8.2).

[3]If two events, A and B are independent then the joint probability is

$$P(A \text{ and } B) = P(A \cap B) = P(A)P(B) \tag{8.1}$$

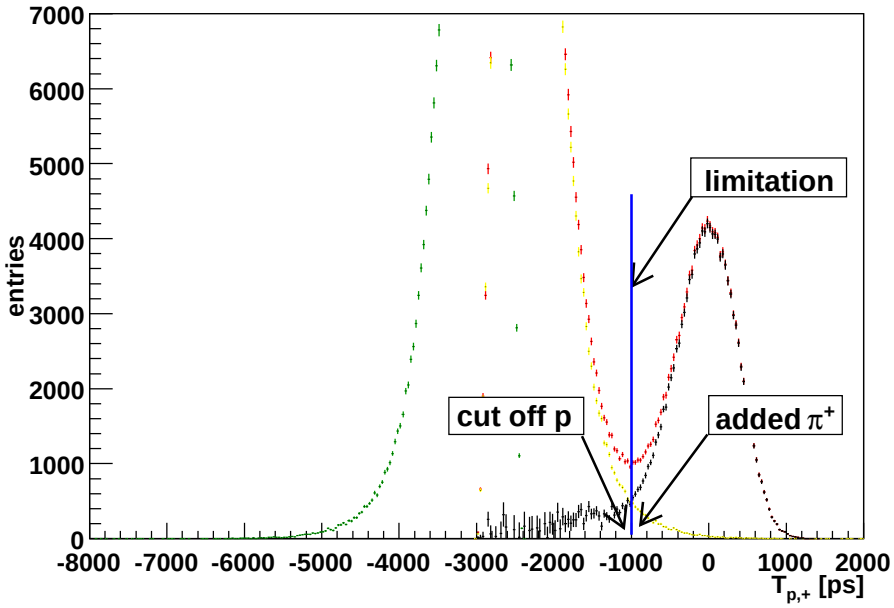

Figure 8.6: Illustration of calculating percents of cut off protons and percents of added π^+ for positive arm for momentum interval p=(2000,2200)MeV/c. The blue line means the time limitation for this momentum interval ($T_{P,+}$ > -1000ps).

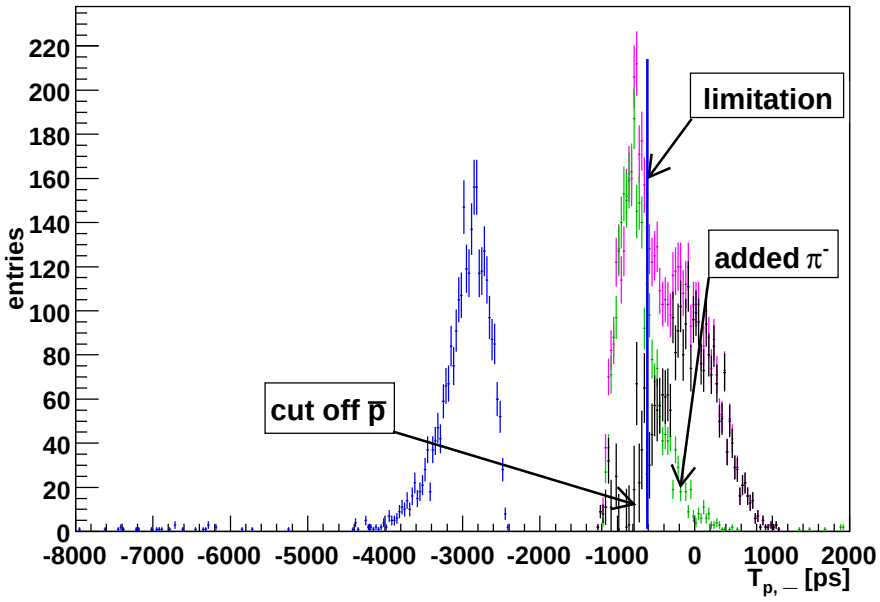

Figure 8.7: Illustration of calculating percents of cut off antiprotons and percents of added π^- for negative arm for momentum interval p=(2000,2200)MeV/c. The blue line means the time limitation for this momentum interval $T_{P,-}$ > -600ps.

momentum interval [MeV/c]	**entries1**	**sse1**	**ratio1** [%]	**entries2**	**sse2**	**ratio2** [%]	**add** [%]	**cut off** [%]
1600-1800	258	±16	0.04	780	±28	0.02	deter.	imposs.
1800-2000	427	±21	0.05	1191	±35	0.03	0.10	1.34
2000-2200	859	±29	0.11	1706	±41	0.04	0.42	2.68
2200-2400	1461	±38	0.19	2261	±48	0.05	1.29	7.86
2400-2600	2603	±51	0.37	3383	±58	0.09	1.28	14.54
total	**5608**	**±75**	**0.15**	**9324**	**±97**	**0.05**		

entries1...number of $p\bar{p}$ pairs with condition $|\Delta t_\pi|$<500ps
entries2...number of $p\bar{p}$ pairs with condition $|\Delta t_P|$<500ps
sse1...standard statistic error for entries1
sse2...standard statistic error for entries2
cut off...percentage of cut off $p\bar{p}$ pairs
add...percentage of added additional pairs
ratio1...percents of $p\bar{p}$ pairs in all pairs of appropriate interval
ratio2...percents of $p\bar{p}$ pairs in $\pi^+\pi^-$ pairs

Table 8.2: Statistic and systematic errors of number of $p\bar{p}$ pairs in individual momenta intervals.

Chapter 9

Conclusion

Data, which were collected in 2001 on nickel targets, were analysed in this work. We tried to find out an admixture of protons, antiprotons and $p\bar{p}$ pairs in these data.

The analysis of protons and antiprotons was done with the help of proposed method "a turning of a peak". The method is based on a turning a half of peak around its mean and on subtraction of behaviours of obtained distributions. For antiprotons are used additional time cuts to cut off unadvisable pions, because antiprotons are not else visible (their number is in data very small). Results of this method are very satisfactory and are mentioned with corresponding statistic and systematic errors in Table (6.1) which relates to protons and in Table (6.2) which relates to antiprotons.

Total number of protons is about 1 037 000 which is approximately 12% from total number of particles in positive arm and total number of antiprotons is about approximately 0.5% from total number of particles in negative arm.

For obtaining the number of $p\bar{p}$ pairs are applied 2D histograms where we combined informations from negative and positive arms together. Conditions of time in negative and positive arm and conditions of $\Delta t_{\pi,p}$ (a difference between outgoing time from the target for positive and negative particle (π - pions or p - anti/protons)) are used for separation these pairs. Received results with errors are presented in Table (8.2).

Total number of $p\bar{p}$ pairs is about 9300 which is approximately 0.05% from total number of pairs and total number of $p\bar{p}$ pairs in $\pi^+\pi^-$ pairs is about 5600 which is approximately 0.15%.

Here introduced results are very important for better off-line analysis of measured data and will be published on DIRAC conferences and DIRAC proposal.

Bibliography

[1] Adeva B. *et al.* - DIRAC proposal, CERN/SPSLC 95-1 (1995).

[2] Gasser J. *et al.* - Phys. Rev. D 64(2001) 016008.

[3] Nemenov L. - Yad. Fiz. 48(1985) 980.

[4] Colangelo G., Gasser J. and Leutwylerb H. - Nuc. Phys. B603 (2001) 125.

[5] Pislak S. *et al.* - Phys. Rev. D 67(2003) 072004.

[6] Schütz Ch.P. - DIRAC thesis "Measurement of the breakup probability of $\pi^+\pi^-$ atoms in a Nickel target with the DIRAC spectrometer" (2004).

[7] Adeva B. *et al.* - Nucl. Instr. Meth. A515(2003) 467.

[8] Gallas M. *et al.* - DIRAC Internal Note 1998-06 (1998).

[9] Adeva B. *et al.* - Nucl. Instr. Meth. A491(2002) 41.

[10] Lanaro A. - DIRAC Internal Note 2002-03 (2002).

[11] Afanasyev L. *et al.* - Nucl. Instr. Meth. A491(2002) 376.

[12] Vlachos S. - DIRAC Internal Note 2003-04 (2003).

[13] Kokkas P. *et al.* - Nucl. Instr. Meth. A471(2001) 358.